Incorporating DFIG-Based Wind Power Generator in Microgrid Frequency Stabilization

by

Mohammadreza Fakhari Moghaddam Arani

A thesis
presented to the University of Waterloo
in fulfillment of the
thesis requirement for the degree of
Master of Applied Science
in
Electrical and Computer Engineering

Waterloo, Ontario, Canada, 2011

AUTHOR'S DECLARATION

I hereby declare that I am the sole author of this thesis. This is a true copy of the thesis, including any required final revisions, as accepted by my examiners.

I understand that my thesis may be made electronically available to the public.

Abstract

Although wind power as a renewable energy is assumed to be an all-round advantageous source of energy, its intermittent nature can cause difficulties, especially in the islanding mode of operation. Conventional synchronous generators can help to compensate for wind fluctuations, but the slow behavior of such systems may result in stability concerns.

In this study, the virtual inertia method, which imitates the kinetic inertia of a synchronous generator, is used to improve the system's dynamic behavior. Since the proposed method incorporates no long-term power regulation, it requires no mass storage device and is thus economical. To preclude additional costs, a rotating mass connected to the Doubly Fed Induction Generator (DFIG) shaft or a super-capacitor connected to the DC-link on a back-to-back converter of a wind power generator could be used.

The concept and the proposed control methods are discussed in detail, and eigen-value analysis is used to study how the proposed method improves system stability. As well, the advantages and disadvantages of using DFIG rotating mass or a super-capacitor as the virtual inertia source are compared. The proposed approach also shows that while virtual inertia is not incorporated directly in long-term frequency and power regulation, it may indirectly enhance the system's steady-state behavior. A time domain simulation is used to verify the results of the analytical studies.

Acknowledgements

First and foremost, I like to thank my supervisor, Professor Ehab El-Saadany for his guidance and kind support throughout my graduate studies. His approach and teaching has inspired me to continue my graduate studies.

My deep gratitude also goes out to all of the members of my family, for the wonderful support they have provided me, especially my mother, Farzane Ameli, and my father, Abbas Fakhari Moghaddam Arani.

As well, I would like to thank my friends in our research group at the University of Waterloo, Aboelsood, Ayman, Hany, Hatem, Mohamed, Morad, Mostafa and Rashed, who contributed so wonderfully to my learning experience.

And finally, I wish to thank all of my dear friends who have enriched my life beyond my studies, especially Farhad Haghighi-zadeh.

To my dear parents.

Table of Contents

List of Figures

List of Tables

.

Chapter 1
Introduction

1.1 Preface

Distributed Generation was introduced as a solution to many difficulties in power systems, such as constructing new transmission and generation units, incorporating renewable energies, and so on. Among these difficulties, improving power reliability is one of the most important issues. It has drawn the attention of many researchers and resulted in the concept of the microgrid. As its name implies, a microgrid allows a part of a distribution system to work in islanding mode in addition to the conventional grid-connected mode of operation.

While, from a reliability and economic point of view, the microgrid islanding mode of operation is interesting, stability issues such as frequency and voltage regulation have slowed down the application of this new mode. On the other hand, growing interest in renewable and environmentally-friendly resources leads to high utilization of these sources. The intermittent nature of most installed renewable energy sources further complicates microgrid islanding, especially since classic regulation methods used in conventional power generators cannot be applied to these undispatchable energy sources.

The situation becomes even more complicated when the type of distributed generation is considered. The electronic-interfaced generation unit, which constitutes the majority of distribution generation units, is assumed as a non-inertia generation. Though these units are much faster than machinery generations to be controlled, they lack inertia, which plays an important role in system stability.

All of these conditions and drawbacks have motivated us to propose a solution for microgrid stability issues in which renewable energies could also participate in frequency regulation. This solution should solve the lack of inertia while at the same time be economical.

To satisfy the above-mentioned constraints, a method which emulates inertia in a conventional generator is introduced. This solution not only compensates for the lack of inertia, but also uses short-term energy sources that are cheaper. Wind power, which is expected to comprise a large portion of distributed generation in the near future, is selected to be modified. The presence of machinery and electronic-interfaced parts simultaneously, and the direct connection of both to a network in conventional wind generation units, provides unique options for implementing the proposed solution.

1.2 Thesis Objective

The main objective of this thesis is to implement a control method in a wind power generation unit to mimic the inertia in conventional generators. This control method will use wind power rotating-mass or a super-capacitor connected to wind power's converter DC-link to minimize the cost. In this thesis, the modifications needed to use each of these sources will be presented in detail.

Enhancements made by implementing virtual inertia will also be discussed in detail. As well, the important factors which impact their performance, including their advantages and disadvantages, will be illustrated and compared.

1.3 Thesis Outline

The thesis is organized as follows. Chapter 2 presents a literature survey on previous work conducted in the areas of load sharing and frequency regulation in microgrids. Chapter 3 is devoted to modifications that should be implemented in a conventional wind power generator control to implement virtual inertia on each of the proposed sources. The modeling of this new wind power generator, its impacts on system stability, and the advantages and disadvantages of each method will be discussed in Chapter 4. Chapter 5 will show the results of a time domain simulation that is used to verify what was discussed in the preceding chapters. Finally, in Chapter 6, conclusions will be drawn and some possible directions for future work will be provided.

Chapter 2
Literature Survey

2.1 Introduction

Power systems operator and planners currently face significant difficulties. On one hand, increasing customer usage is forcing utilities to increase their generation capacity for higher quality sustained power. On the other hand, erecting new transmission lines and building new plants can be a formidable task, with substantial negative economic and environmental repercussions. Consumer demand for renewable and environmentally-friendly energy sources that do not emit pollutants is yet another important challenge that today's power systems must contend with.

Distributed generation (DG) is a promising solution being investigated by researchers. DG not only reduces on-peak operation costs, improves reliability and voltage profile, and incorporates renewable energy, but it can also defer or even remove the need to upgrade transmission systems [1], [2].

A microgrid is defined as a cluster of distribution systems that contains DG and can operate both in grid-connected mode and autonomously [3]. It is known as an appropriate way to incorporate DG in a distribution system. Although a microgrid can work in grid-connected mode and have many benefits, its most important impact is reliability enhancement due to its islanding operation [4]. Consequently, many papers have been published in this area. The most important issue for the successful operation of a microgrid in islanding mode is retaining frequency and voltage in an allowed range while providing sufficient power to loads [5]. Investigations show that these topics can be in close relation [6].

In this chapter, load sharing and its methods will be reviewed first, followed by a discussion on wind power. Next, some of the difficulties encountered in extracting maximum available wind power and incorporating it into a microgrid will be delineated. This will be followed by an investigation of the methods proposed to improve microgrid frequency behavior in the presence of wind. Finally, similar work available in the literature will be presented and critiqued.

2.2 Load Sharing

Load-sharing methods can be classified into two major categories. The first is communication-based methods, which require communication channels among DG units. The second category is droop-based methods, in which DG units use system parameters, locally available, to regulate power and frequency.

2.2.1 Communication-Based Methods

In this form of load sharing, DG units are classified into two different types based on their control methods: PQ-controlled DG units and voltage-controlled DG unit. PQ-controlled DG units produce pre-specified P and Q. They track the network voltage and frequency and can be modeled as current sources [7]. Voltage-controlled DG units are modeled as voltage sources. They are responsible not only for voltage and frequency regulation, but also for sudden changes in load or generation. Thus, they are usually a kind of energy storage devices interfaced by an inverter [7], [8].

VSI DG works as a master unit and regulates both network voltage and frequency. It also sends reference working points to slave DG units (PQ-type). This reference value can be in the form of reference current value [9], [10] or, in some cases, PWM signals [9].

Although the communication-based methods have advantages such as the ability to function smoothly regardless of line impedance and network topology, many disadvantages, such as the need for communication circuits, less reliability, more complexity, and higher cost, have made this class relatively unpopular [9]-[13]. Moreover, in many systems, only one master unit exists, which means the system is highly dependent on this unit. This can exponentially worsen emergency situations, considering that the master unit's role is to respond to sudden changes in loads [10], [14].

Various attempts have been made over the years to improve communication-based methods. [9] suggests using wireless communication, which eliminates the need for extra circuits. However, this method suffers from delays, noise, interference and channel nonlinearity, all of which negatively impact performance. Multi-Master Operation (MMO), where several DG units work as master units, has better reliability and more stable behavior in the case of sudden changes in load [7]. Demand-side management and load-shedding in case of emergency also improve the performance of these methods [7], [8]. In [8], a method is proposed which combines communication and droop methods. While this combination may result in less information transfer (and thus less bandwidth and lower cost), it appears only to be economical for short geographical span microgrids.

2.2.2 Droop-Based Method

The droop method is the most well-known method for load-sharing in microgrids. It emulates the behavior of conventional generators in power systems and uses frequency and voltage of line as a communication tool to share the active and reactive load. It also regulates both the voltage and the frequency at the same time [15]. In this method, only local variables are needed.

As mentioned previously, this method is based on the relationship between power and voltage.

Figure 2.1 illustrates that the relationships between active and reactive power and terminal voltages are:

$$P = \frac{U_1^2}{Z}\cos\theta - \frac{U_1 U_2}{Z}\cos(\theta + \delta) \tag{2.1}$$

$$Q = \frac{U_1^2}{Z}\sin\theta - \frac{U_1 U_2}{Z}\sin(\theta + \delta) \tag{2.2}$$

while $Ze^{j\theta} = R + jX$. With the assumption of $X >> R$ and a small δ, which results in $\sin(\delta) \approx \delta$ and $\cos(\delta) \approx 1$, they can be represented as:

$$\delta = \frac{XP}{U_1 U_2} \tag{2.3}$$

$$U_1 - U_2 = \frac{XQ}{U_1} \tag{2.4}$$

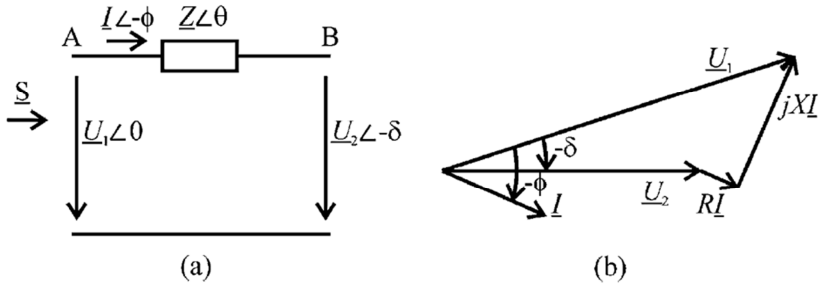

Figure 2.1 (a) Power flow through a line (b) phasor diagram [16]

These linear relations and successful conventional generators lead to defining virtual droop characteristics for electronic interfaced DGs due to regulation of frequency and voltage via active and reactive power, respectively.

$$f - f_0 = -K_p(P - P_0) \tag{2.5}$$

$$U - U_0 = -K_q(Q - Q_0) \tag{2.6}$$

Frequency and voltage can be controlled to remain in limited ranges, and load sharing among DGs is proportional to their droop factors (K_p, K_q).

Specifying droop factors can be based on a range of philosophies. While in references such as [15] and [17]-[20], determining these factors is based on the rating of DG units (like (2.7), in which S is the rated apparent power of DG unit and i, j are the numbers of units), references such as [11], [21] specify them on the basis of maximum allowable deviation in frequency, voltage and maximum output power (like (2.8)). Coefficients also play a role in the dynamic behavior of microgrids, creating some conflicts that may result in the slow behavior of inverter-based DGs.

$$K_{p_i} S_i = K_{p_j} S_j \tag{2.7}$$

$$K_{p_i} = \frac{\Delta f_{allowed}}{P_{i,\max}} \tag{2.8}$$

$$K_{q_i} S_i = K_{q_j} S_j \tag{2.9}$$

$$K_{q_i} = \frac{\Delta V_{allowed}}{Q_{i,\max}} \tag{2.10}$$

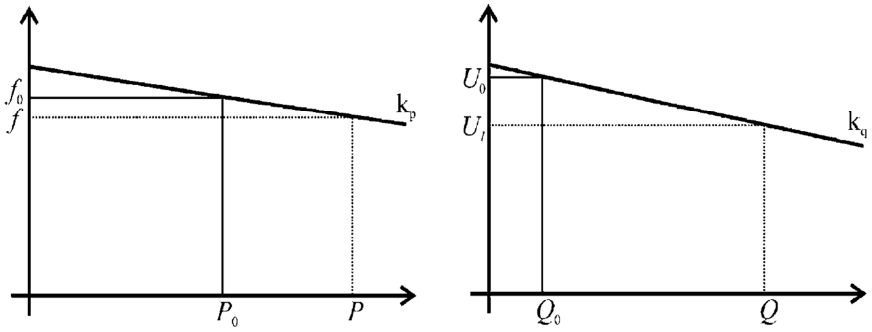

Figure 2.2 Frequency and voltage droop characteristics [16].

The conflict between steady-state and dynamic behavior impacts of droop factors is a significant limitation of this method. Moreover, the relatively low inductive nature of line impedance in many distribution systems violates assumptions which lead to (2.3) and the droop equations, while the presence of nonlinear and unbalanced loads in a distribution system renders these problems all the more complicated. Many researchers have tried to address and resolve these issues [5], [18], [19]; however, the droop method is not applicable to undispatchable sources of energy, which are anticipated to comprise a large portion of DGs' installed capacity.

2.3 Wind power

As one of the world's most important renewable energies, wind power is frequently used in microgrids, but the intermittent behavior of wind introduces some difficulties.

2.3.1 DFIG

To extract the maximum power of the wind with variable speeds, different turbine speeds are needed [3], [21]-[25], as illustrated in Figure 2.3. Synchronous generators connected to a network via an inverter or squirrel cage induction generators have been investigated as solutions, though Doubly Fed Induction Generators (DFIGs) are better known. The stator of this induction generator is directly connected to a network, while its rotor is connected to a network by a back-to-back converter. The

converter has lower rating than the inverter connected to similar synchronous generators [22], [25]. In addition, some other difficulties, such as maximization of output power and providing reactive power, have resulted in the preference of DFIG over squirrel cage induction machines [24], [25].

Each of these two converters in this control method are used to regulate different values. In the grid connected mode, the Grid Side Converter (GSC) is used to regulate the DC link voltage, while the Rotor Side Converter (RSC) is used to maximize the power extraction, since a specified rotor speed corresponding to any wind speed is required [3], [25]. RSC also provides the DFIG with the requisite reactive power.

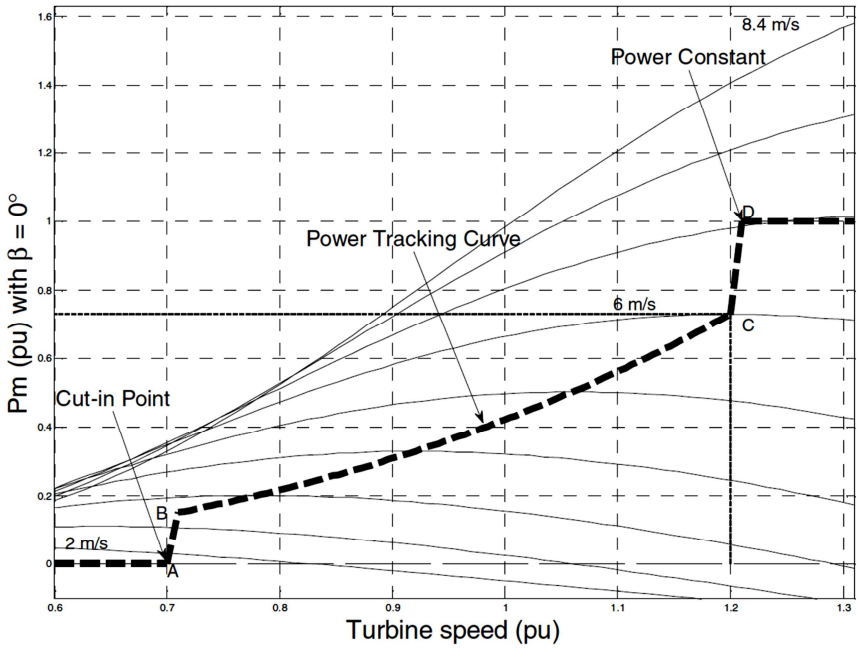

Figure 2.3 A wind turbine characteristic showing that a specified wind speed is required to extract maximum power in each speed. Different curves are related to different wind speeds, and Pm is the mechanical output power of the turbine [25].

2.3.2 Compensating Wind Variability

For the sake of reliability, another source is needed to compensate changes in wind generator output [26]. The interaction of this source with a wind plant, and its impact on system stability and quality, may be significant. Different topologies have been presented for a wind generator. In addition to economic aspects, they should also address and resolve these problems. Various topologies have been presented.

2.3.2.1 Battery

References such as [21] and [22] have proposed using the Grid Side Converter (GSC) to regulate the active power of the generator. To regulate active power, a storage device which is connected to the DC link of the converters is required. The schematic diagram of back-to-back in this method is shown in Figure 2.4.

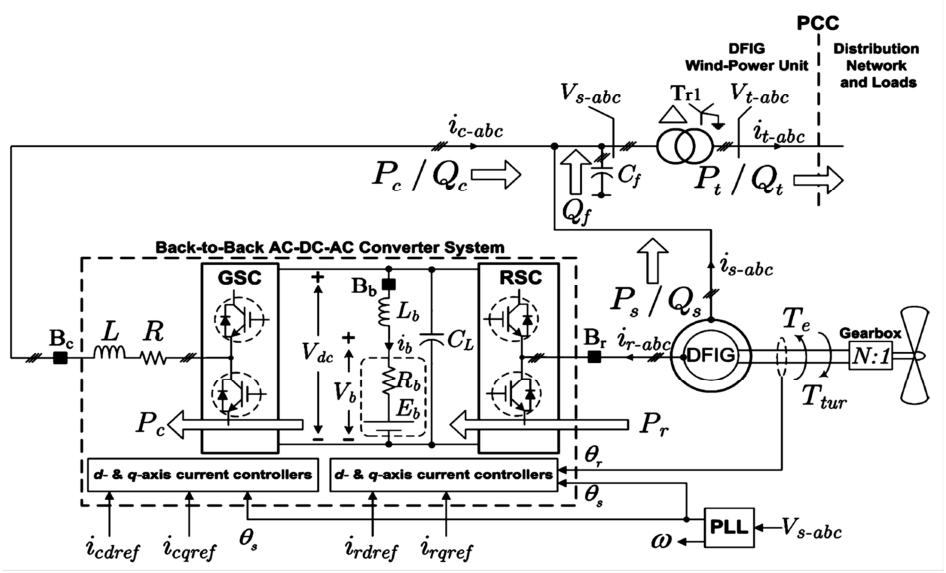

Figure 2.4 Schematic diagram of a DFIG wind power unit. [21].

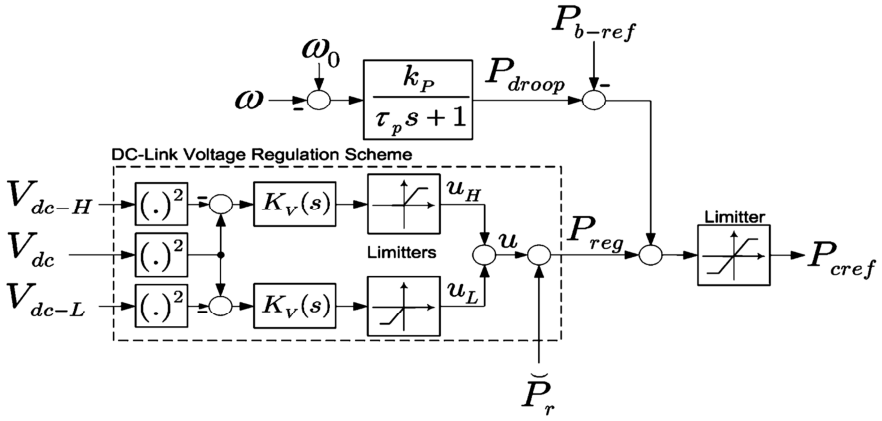

Figure 2.5 Block diagram of GSC real power management. Pr is an estimate of rotor power consumption, and Pb-ref is battery power command and determines the amount of battery power production. Frequency regulation is done by GSC [21].

In Figure 2.5, GSC is also incorporated into the microgrid frequency regulation by implementing a droop equation in its controller. This method, while not removing the intermittency of wind, improves performance. Using the GSC for reactive power regulation, which would result in the

independency of the reactive power generation of wind speed variation, has been suggested [22]. GSC has also been used by [22] to supply the unbalanced loads of microgrids and maintain the DFIG load balance, since negative sequence current negatively impacts DFIG performance. Some drawbacks, especially the battery and higher rated GSC costs, have prevented wide usage of this method [27].

2.3.2.2 Conventional Generators

Some references, such as [28] and [29], prefer to use conventional generators like diesel instead of storage devices and GSC to compensate for wind power variations. Although from a reliability and economic point of view, such a preference makes sense, the stability of the network may be affected, since synchronous generators are slower than electronic interfaced DGs [6], [15].

In [3], where a diesel is used for compensation, an attempt is made to combine the droop and maximum power tracking to regulate the power and frequency faster and better. In this method, P_0 in (2.5) is variable and is the maximum available wind power.

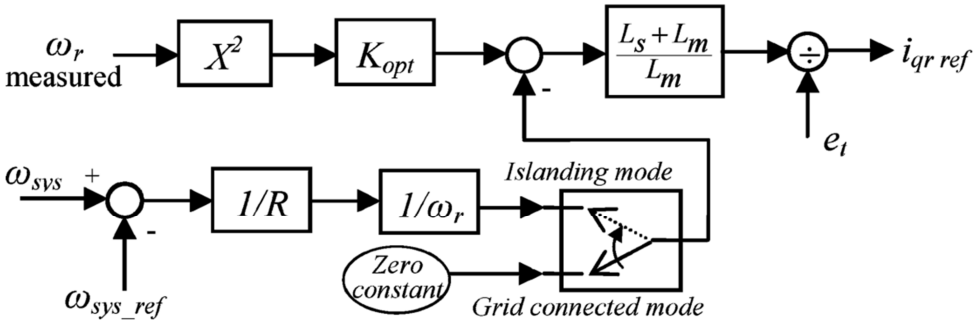

Figure 2.6 Integrated active power and frequency control of DFIG [3]

Although the proposed control method, seems to work well if applied in a system with one dispatchable DG unit (which can restore the frequency to its nominal value), it will have serious problems if multiple dispatchable DG units are used in a microgrid. In such a system, dispatchable DG units share their power based on droop, and consequently, frequency deviation is unavoidable [30].

2.3.2.3 Small-Capacity Storage Device

Using batteries is not economical, and conventional DGs are slow. However, adding small-capacity inexpensive storage devices to synchronous generators can compensate short-term for any limitations of the system's dynamic behavior conflicts [6].

The concept of using a storage device short-term in addition to a conventional generator long-term is used in various models. [31] and [32] utilized a storage device to compensate for wind power variations in short-term disturbances, while a diesel was responsible for the steady state mode. They found that the main problem with using a storage device and inverter separate from the wind generator was additional cost. [27] used GSC to reduce power output variations with respect to prediction. The storage device compensated DFIG in the short-term, leading to the use of lower capacity storage devices, such as super-capacitors, which are more cost-effective. However, the method proposed in [27] uses GSC to mitigate the fluctuations only under grid-connected mode and does not discuss islanding modes and frequency regulation.

2.3.2.3.1 Virtual Inertia

If a disturbance occurs in a conventional power system, the rotating mass of the conventional synchronous generator will provide power in the short-term, making the system more stable. In the synchronous machine, the relation between the input mechanical power, P_m, and the output electrical power, P_e, is described by (2.11), in which ω_m and J are the angular velocity of the rotor and the moment of inertia of the rotating mass connected to the rotor, respectively. Thus, if a disturbance occurs in the system, the rotating mass of the generator will provide the power in the short term to make the system more stable. In steady-state, where the frequency is settled and constant, the derivative term is zero.

$$P_m - P_e = \frac{d}{dt}\left(\frac{1}{2} J\omega_m{}^2\right) = J\omega_m \frac{d\omega_m}{dt} \tag{2.11}$$

The idea of emulating this behavior in non-inertia inverter-based DG units, which form the major portion of DG resources [33]-[34], has been employed by several researchers. For instance, [14] and [18] implemented the method by adding a derivative term of frequency to droop equations to improve the dynamic behavior of systems. This solution allowed them to solve the dynamic conflicts of the droop factor, discussed in section 2.2.2., but only in dispatchable DGs. Later references, such as [35] and [36], used virtual inertia explicitly.

Although some researchers have employed virtual inertia in undispatchable DGs, most use this control method in the grid-connected mode [35]-[40]. Even in reference [41], which discusses islanding, virtual inertia is implemented in a separate inverter; moreover, the energy storage device connected to this inverter is assumed to have no limit.

In a wind power generator, two sources for implementing this virtual inertia can be considered. One is the rotating mass connected to the rotor of DFIG [38], [40]. Using this source does not impose any new costs for new hardware. In the conventional control method of DFIG, this rotating mass does not participate in frequency regulation [40]. While references [38] and [40] have implemented this idea before, no stability analysis has been presented to show how the method enhances system behavior or which factors affect the method's performance.

The other way to implement virtual inertia is to use a super-capacitor connected to the DC link of the back-to-back converter controlling the DFIG. While this method removes the cost of a new inverter, it has not yet been implemented in the GSC of wind power.

In this work, both sources will be utilized. The requisite modifications in controllers will be discussed and compared in different aspects.

2.4 Discussion

In this chapter, various approaches to microgrid frequency regulation were reviewed. The communication-based methods and droop-based methods, as the most well-known classes of load-sharing, were studied, along with the main reasons why they cannot be used in wind power generation. Using battery and conventional DGs as two options for compensating wind power generation were investigated, and the advantages and disadvantages of using each of those options and proposed modifications in the literature were discussed.

As well, the benefits of short-term utilization of small storage devices, in addition to conventional DG units, were discussed in detail. Virtual inertia as a useful control method was introduced, and the concept, previous works and their drawbacks were reviewed. Finally, possible sources for implementing this method were investigated.

Chapter 3
Wind Based DG Controller

A wind power generator is shown in Fig. 1. In conventional configurations, the ESS and the switches connecting it to the DC-link are absent. The RSC is used to extract the maximum available wind power and regulate the stator voltage, while the GSC is responsible for regulating the DC-link voltage.

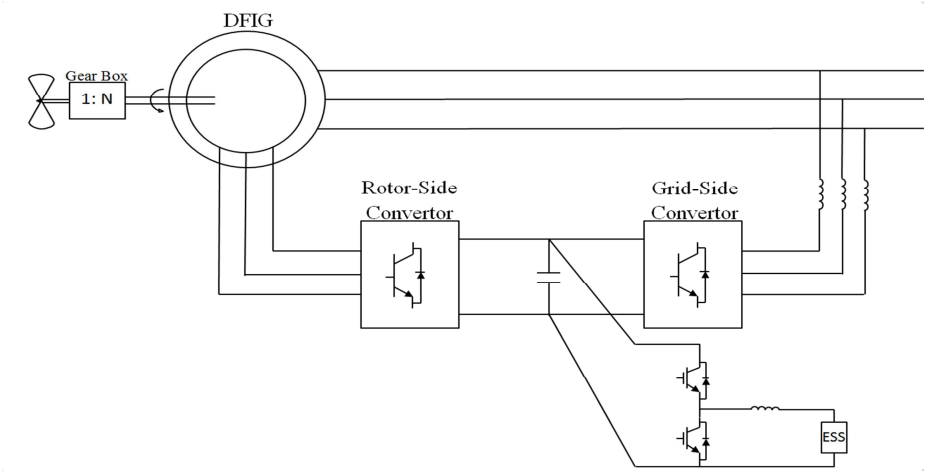

Figure 3.1Wind Power Generator

The following section discusses the controller and modifications needed to incorporate each of these two short-term energy sources.

3.1 Rotor Side Converter Controller

RSC control in islanding mode is similar to the control method used in grid-connected mode. However, where DFIG is controlled to maximize the active power extraction in both cases, the reactive power controller differs. DFIG is expected to work at the unity power factor in grid-connected mode, while it is used to regulate the stator bus voltage in islanding mode. Here, the method based on discussions in [42] and [3] is employed.

3.1.1 DFIG controlling

The DFIG voltages and current can be presented by equations (3.1)-(3.4) [43]:

$$v_{ds} = -R_s i_{ds} - \omega_s \psi_{qs} + \frac{d\psi_{ds}}{dt} \tag{3.1}$$

$$v_{qs} = -R_s i_{qs} + \omega_s \psi_{ds} + \frac{d\psi_{qs}}{dt} \tag{3.2}$$

$$v_{dr} = +R_r i_{dr} - s\omega_s \psi_{qr} + \frac{d\psi_{dr}}{dt} \tag{3.3}$$

$$v_{qr} = +R_r i_{qr} + s\omega_s \psi_{qr} + \frac{d\psi_{dr}}{dt} \tag{3.4}$$

where ω_s and ω_m are synchronous and rotational speed, respectively and s, r and m subscripts differentiate stator, rotor and mutual parameters. Slip (s) and flux (ψ) used in the above equations are defined as below:

$$\psi_{ds} = -(L_s + L_m) i_{ds} + L_m i_{dr} \tag{3.5}$$

$$\psi_{qs} = -(L_s + L_m) i_{qs} + L_m i_{qr} \tag{3.6}$$

$$\psi_{dr} = +(L_r + L_m) i_{dr} - L_m i_{ds} \tag{3.7}$$

$$\psi_{qr} = +(L_r + L_m) i_{qr} - L_m i_{qs} \tag{3.8}$$

$$s = \frac{\omega_s - (P/2)\omega_m}{\omega_s} \tag{3.9}$$

To control the DFIG active power output, the rotor voltages or currents should be controlled in such a way that either the output active power or the electrical torque tracks the reference value.

$$T_e = \psi_{dr} i_{qr} - \psi_{qr} i_{dr} \tag{3.10}$$

To simplify the controller, some assumptions can be made. First, the d-q frame could be chosen in-phase with the DFIG stator voltage so that v_{qs} will be zero. The stator resistance could be neglected and the steady-state conditions considered. The last assumption will lead to ignoring the derivative terms in equations (5)-(9). After implementation of these simplifications, the electrical torque can be expressed as a function of rotor voltage:

$$T_e = \frac{L_m v_{ds}}{\omega_s (L_s + L_m)} i_{dr} \tag{3.11}$$

Now, by replacing $T_{e\text{-}ref}$ in equation (5), the desired value of i_{dr}, which results in the optimal torque, can be derived:

$$i_{dr-ref} = \frac{\omega_s (L_s + L_m)}{L_m v_{ds}} T_{e-ref} \tag{3.12}$$

These assumptions also let us rephrase the output reactive power of the DFIG stator as a function of the rotor current.

$$Q_{stator} = v_{ds}\left(\frac{v_{ds}}{\omega_s(L_m + L_s)} + \frac{L_m}{L_s + L_m} i_{qr}\right) \tag{3.13}$$

Reference [3] proposes dividing i_{qr} into two in-phase components, $i_{qr,mag}$ and $i_{qr,gen}$, in which the former is responsible for magnetizing the generator and the latter specifies the net reactive power exchange between the DFIG stator and the grid. To provide the required total magnetizing reactive power of DFIG, $i_{qr,mag}$ should be determined such that $i_{qr,gen}$ and Q_{stator} are zero. After replacing these two parameters by zero, the desired value of $i_{qr,mag}$ will be obtained, as shown in (3.15).

$$i_{qr} = i_{qr,mag} + i_{qr,gen} \tag{3.14}$$

$$i_{qr,mag-ref} = -\frac{v_{ds}}{\omega_s L_m} \tag{3.15}$$

In grid-connected mode, where the unity power factor performance is desired, $i_{qr,gen-ref}$ is set to zero, but in islanding mode, it is used to regulate the bus voltage, as shown in Figure 3.2.

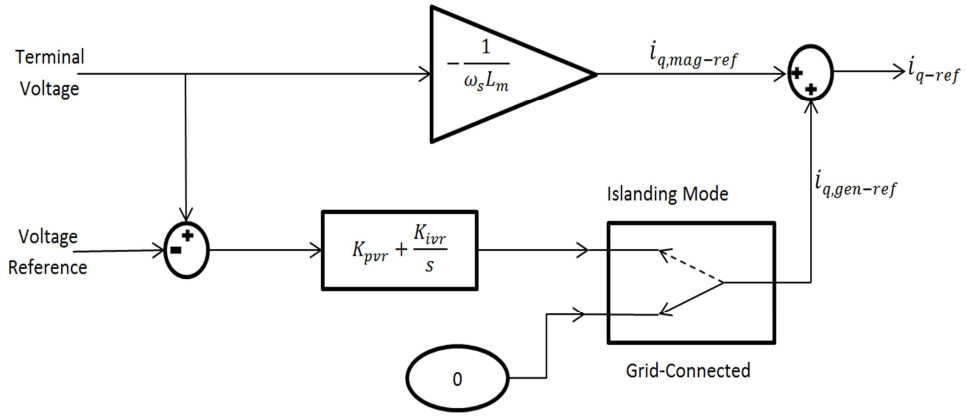

Figure 3.2 Reactive power controller

3.1.2 Active Power Regulation

In general, the optimum power that can be extracted from a wind turbine is obtained from (3.16).

$$P_{opt} = 0.5\rho C_{P,opt}(\lambda_{opt}, \theta) A_r v_w^{\ 3} \tag{3.16}$$

where ρ is the air density, $C_{P,OPT}$ is the optimal power coefficient of the wind turbine, λ_{opt} is the optimal tip ratio, θ is pitch angle, A_r is effective area covered by the turbine blades, and v_w is wind speed. This equation can be represented as:

$$P_{opt} = K_{OPT}\omega_r^{\,3} \tag{3.17}$$

where K_{OPT} is associated with blade angle and can be considered constant if the pitch angle is kept unchanged. Based on this equation and the relation between power and torque, the desired value of T_e can be obtained.

$$T_{e,opt} = K_{OPT}\omega_r^{\,2} \tag{3.18}$$

The RSC controller tries to track this value as quickly and accurately as possible. In other words, if the controller is fast enough, it can be assumed that the electrical torque, T_e, is equal to $T_{e,OPT}$. In the next section, the accuracy of this assumption will be discussed.

$$T_e = K_{OPT}\omega_r^{\,2} \tag{3.19}$$

In a conventional generator in which the input mechanical power, instead of the electrical output power, is controlled by a governor, the inertia relation can be represented as in (3.20). In these generators, a derivative term which introduces the rotating mass inertia and depends on the system frequency, is also incorporated directly into the generator output power. In a wind-powered generator where T_m is undispatchable and ω_r is not dependent on the system frequency, T_e is controlled directly, so the rotating mass has no impact on the frequency regulation.

$$T_e = T_m - J\frac{d\omega_m}{dt} \tag{3.20}$$

To involve DFIG rotating mass in the frequency regulation, the controller should mimic (3.20), and thus equation (3.18) should be modified to equation (3.21). $H_V(s)$ represents the virtual inertia and will be discussed later in more detail.

$$T_{e,ref} = K_{OPT}\omega_r^{\,2} - H_V(s)\omega_m \tag{3.21}$$

3.1.3 Current Controller

Based on the desired torque and stator voltage, the desired values of d and q current component can be calculated. These reference values of currents will later be used to produce desired rotor voltage. As seen in Figure 3.3, they actually produce the modulation signals, which are used in PWM drivers to generate the gate pulses for switches.

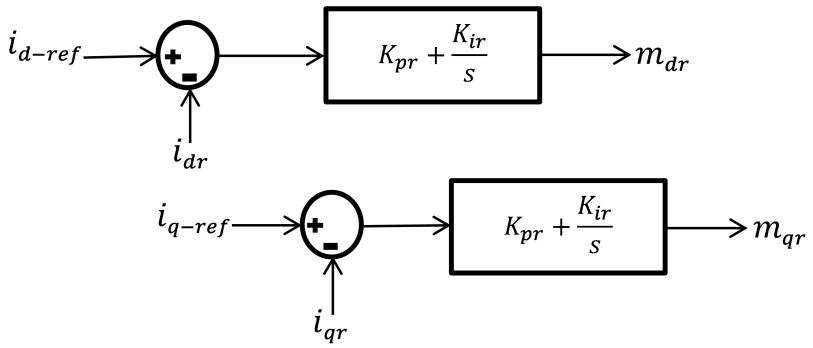

Figure 3.3 PI controllers of RSC

3.2 Grid Side Converter Controller

3.2.1 Active Power Regulation

3.2.1.1 Super-Capacitor via a DC/DC convertor

In the model shown in Figure 3.1, GSC should maintain a constant DC link voltage. In (3.22), the relation between $V_{dc\text{-}link}$, the DC-link capacitor voltage; P_{gsc}, GSC output power; and P_{rsc}, RSC needed power is presented. Due to the lack of a mass storage device in the DC link, the GSC should provide the needed energy of the RSC as quickly as possible.

$$P_{rsc} - P_{gsc} = \frac{1}{2} C_{dc-link} \frac{d(V_{dc-link}{}^2)}{dt} \tag{3.22}$$

By adding a super-capacitor and its convertor to the DC-link, (3.22) should be rephrased as (2.23). P_{scap} is the power injected into the super-capacitor:

$$P_{rsc} - P_{gsc} - P_{scap} = \frac{1}{2} C_{dc-link} \frac{d(V_{dc-link}{}^2)}{dt} \tag{3.23}$$

If the GSC controller is set to be fast and accurate enough, $V_{dc\text{-}link}$ can be assumed to be constant. In other words, by appropriate control parameter tuning, the right side of (3.23) will be zero. This equation can be represented by (3.24).

$$P_{gsc} = P_{rsc} - P_{scap} \tag{3.24}$$

In addition, the inertia relation in machines, introduced by (2.11), can be simplified as (3.25). This simplification seems to be reasonable, since the frequency always remains very close to its nominal value. The derivative term will be zero in steady-state, while the frequency is constant but not necessarily at its nominal value.

$$P_e = P_m - J\omega_0 \frac{d\omega}{dt} \tag{3.25}$$

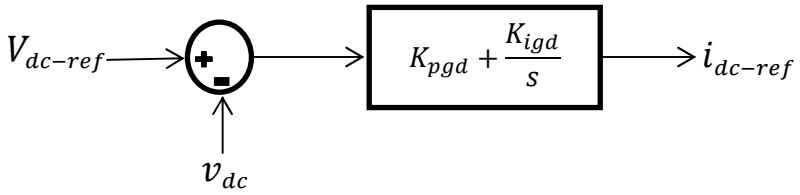

Figure 3.4 DC-Link Voltage regulator

To implement virtual inertia in the GSC controller, P_e,which is the output power of the machine, should be replaced by P_{gsc}, which is the output power of GSC. Further, P_m which is the input power to the machine, should be replaced by P_{rsc} which is the power needed by the rotor terminals of DFIG. The super-capacitor will be responsible for mimicking the rotating mass behavior. This new relation is shown in equation (3.26). $H_V(s)$, as in equation (3.21), is an emulation of a derivative.

$$P_{scap} = H_V(s)\omega_0\omega_m \tag{3.26}$$

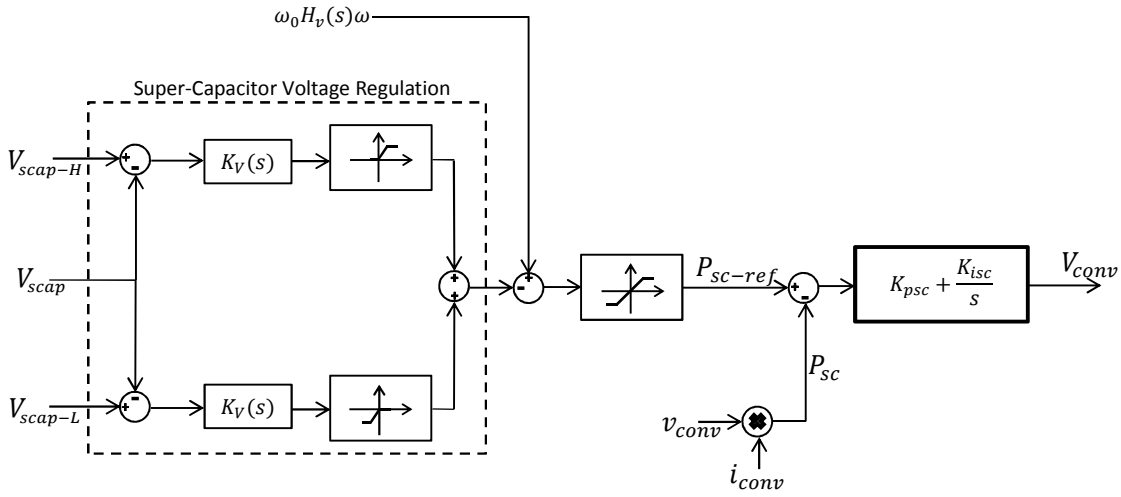

Figure 3.5 Super-Capacitor Controller

3.2.1.1.1 Super-Capacitor Controller

A Super-Capacitor should be controlled quickly and accurately to generate virtual inertia power, especially since this power is needed in transient mode. However, the fast and accurate tracking of the virtual inertia is not the only responsibility of this controller. It should also keep the Super-Capacitor voltage in a limited range and prevent any under- or over-voltage. Although designing the Super-

Capacitor (discussed in the next chapter) is based on retaining its voltage within the limit range, this controller is also used as a back-up. Figure 3.5 shows the block diagram of the super-capacitor controller.

3.2.1.2 Super-Capacitor directly connected to DC-link

The Super-Capacitor can also be connected directly to a DC-link. In this method, the GSC active power controller should be modified to provide RSC needed power and virtual inertia power. A GSC controller block-diagram is shown in Figure 3.6.

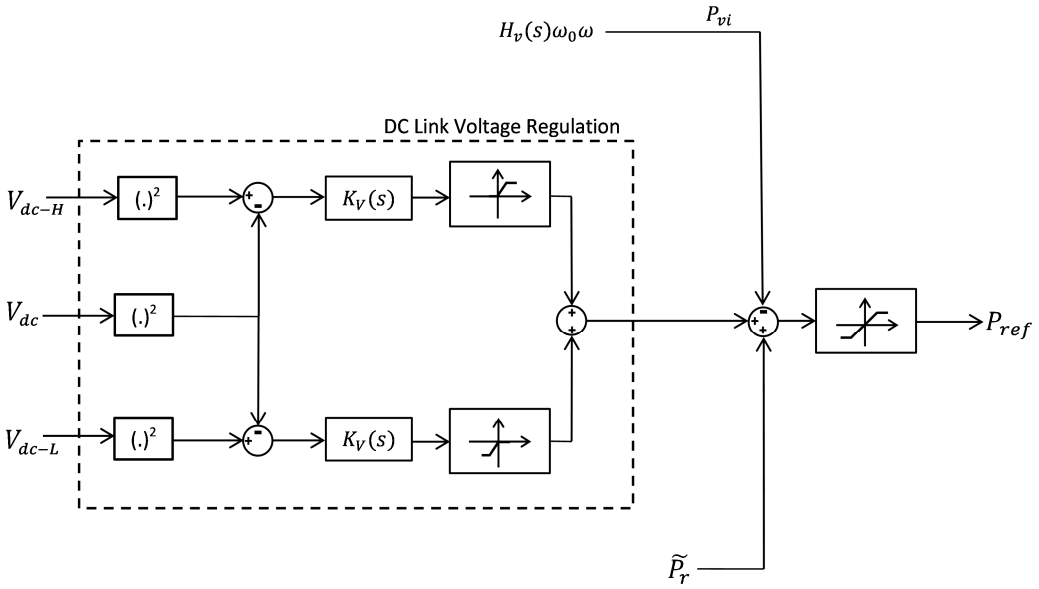

Figure 3.6 Power Controller Block of GSC Controller

This block diagram has a DC link voltage regulating block in addition to what has already been discussed. This block tries to regulate the capacitor voltage within a reasonable range. In fact, it prevents violation of DC link voltage limits that may occur due to use of the virtual inertia method. Later, the generated P_{ref} will be used to produce $i_{d\text{-}ref}$. It is worth noting here that the rest of the controller is exactly the same.

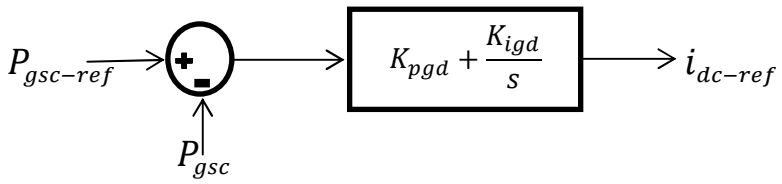

Figure 3.7 Active Power Regulations

However useful and economical this topology seems to be because the DC/DC converter is removed, the former topology may yet be preferred. Fluctuating DC-link voltage is a major disadvantage of this topology that will be discussed later in detail. The other point is the GSC dependence on a super-capacitor. In the former topology, if a fault in the super-capacitor or the DC/DC converter takes place, GSC and consequently the wind power plant can still work, with no modifications in the controller, just by disconnecting the faulted part. Although in this case no virtual inertia is implemented, the wind power plant can work as a conventional one. In the latter case, the situation is different and modifications to the controller parameters are necessary.

3.2.2 Reactive Power Regulation

To avoid interference between GSC and DFIG, GSC is controlled to work at the unity power factor. Since the d-q frame is chosen such that v_{qs} is zero, the reactive power could be controlled by regulating the i_q. Figure 3.8 shows the reactive power regulation block.

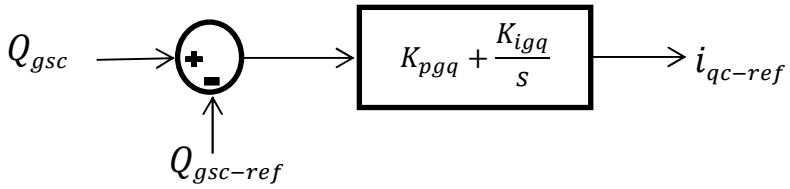

Figure 3.8 Reactive Power Regulation

3.2.3 Current Controller

The current reference values generated in the previous sections are used to regulate the current. Figure 3.9 shows GSC connection to the network. Equation (3.27) describes the relation between the current and voltages shown in Figure 3.9.

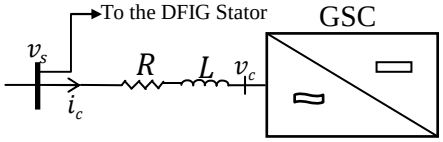

Figure 3.9 GSC Connection to network

$$\frac{d}{dt}\begin{bmatrix} i_{cd} \\ i_{cq} \end{bmatrix} = \begin{bmatrix} -\frac{R}{L} & \omega_s \\ -\omega_s & -\frac{R}{L} \end{bmatrix}\begin{bmatrix} i_{cd} \\ i_{cq} \end{bmatrix} + \frac{1}{L}\begin{bmatrix} v_{sd} - v_{cd} \\ v_{sq} - v_{cq} \end{bmatrix} \tag{3.27}$$

As can be seen, the current components are coupled. To eliminate this coupling (based on what [6] has proposed), a new parameter, v', will be introduced so that (3.27) can be represented as (3.29). According to this new equation, the controller shown in Figure 3.10 is designed thus:

$$\begin{bmatrix} v'_d \\ v'_q \end{bmatrix} = \omega_s L \begin{bmatrix} i_{cq} \\ -i_{cd} \end{bmatrix} + \begin{bmatrix} v_{sd} - v_{cd} \\ v_{sq} - v_{cq} \end{bmatrix} \tag{3.28}$$

$$\frac{d}{dt}\begin{bmatrix} i_{cd} \\ i_{cq} \end{bmatrix} = \begin{bmatrix} -\frac{R}{L} & 0 \\ 0 & -\frac{R}{L} \end{bmatrix} \begin{bmatrix} i_{cd} \\ i_{cq} \end{bmatrix} + \frac{1}{L}\begin{bmatrix} v'_d \\ v'_q \end{bmatrix} \tag{3.29}$$

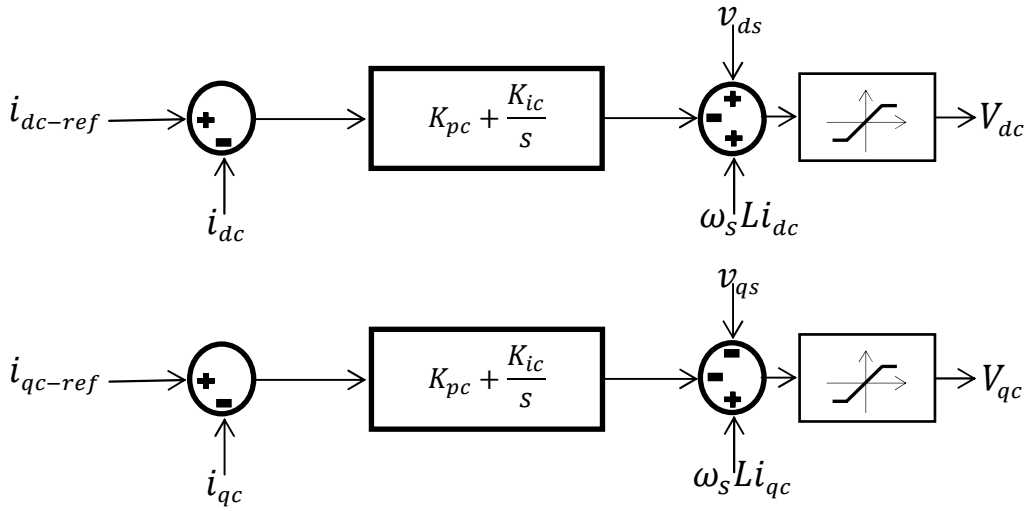

Figure 3.10 GSC Current Controller block diagrams [6]

3.3 Implementing Virtual Inertia

As mentioned, due to the practical concerns of a simple derivative, $H_V(s)$ is represented as (3.30). In low frequencies, $H_V(s)$ behaves similar to the derivative while its performance on high frequencies is different.

$$H_V(s) = \frac{J_V s}{(\tau_1 s + 1)(\tau_2 s + 1)} \tag{3.30}$$

To generate $H_V(s)\omega$, the Phase Locked Loop (PLL) technique is used. The block diagram of a PLL is shown in Fig. 3.11. Based on what [28] has proposed, equation (3.31) can be derived, where V_p is the peak voltage of V_{abc}. If the loop filter is chosen to be a PI controller such as (3.32), then (3.30) can be represented as (3.33).

$$v_q = \frac{V_p}{s + K_f(s)V_p}\omega \tag{3.31}$$

$$K_f(s) = K_{pll} + \frac{K_{ill}}{s} \tag{3.32}$$

$$v_q = \frac{s}{\frac{1}{V_p}s^2 + K_{pll}s + K_{ill}}\omega \tag{3.33}$$

This new equation is very similar to (3.30). By choosing the proper K_{pll} and K_{ill}, as illustrated in [44], v_q, which is already generated and needed for the other parts of the DG controller, can be used to produce $H_V(s)\omega$.

$$H_V(s)\omega = J_V K_{ill} v_q \tag{3.33}$$

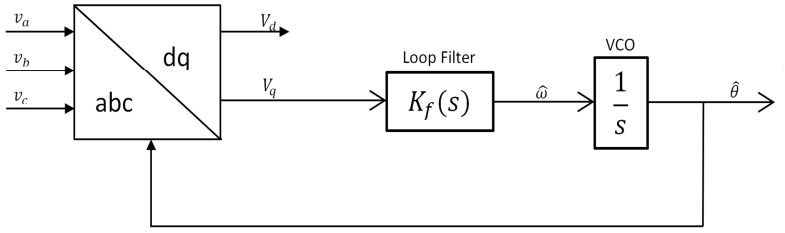

Figure 3.11 PLL block Diagram

3.4 Discussion

In this chapter, the wind power generator controller was presented in detail. The RSC conventional controller, which is responsible for extracting the maximum available wind power and regulating the stator voltage, was studied and then modified to use DFIG rotating-mass as the source of virtual inertia. The two possible topologies for connecting the Super-Capacitor and GSC controllers, which are responsible for regulating the DC-link voltage in conventional wind generators, have also been discussed. Finally, a method for implementing virtual inertia was presented.

Chapter 4
Stability Analysis

Further analysis is needed to verify that virtual inertia can improve system stability. In Fig. 4.1, a typical rural distribution system is considered. The segment after the circuit breaker B2 has the ability to work in islanding mode and constitutes the microgrid. The overall load of this section is 3.77MW plus 1.24MVAR, and it contains two DG units. DG1 is a variable-speed wind turbine connected to a 2.5MVA DFIG with its rotor interfaced by a back-to-back converter. DG2 represents a 2.5MVA conventional gas-turbine generator equipped with droop-based governor and excitation control systems.

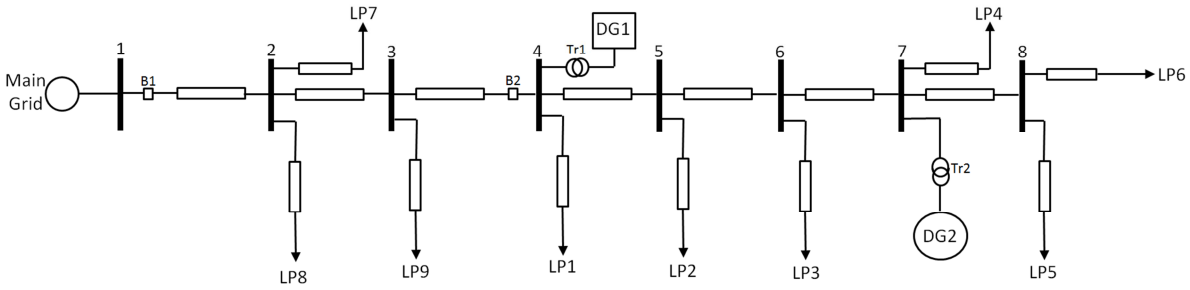

Figure 4.1 The System under Study

4.1 Wind Power

To study virtual inertia's impact on system stability, an accurate model of wind power is needed. Thus, a detailed model will be provided here. Although the model is accurate, its complexity makes the stability analysis messy and complicated. To overcome these problems, a simplified model will be extracted that makes analysis easier while still being accurate.

In this section, a detailed model of wind power where virtual inertia has not yet been implemented will first be obtained, after which this model will be used to construct a simplified model and implement the virtual inertia.

4.1.1 Detailed Model

In this section, a wind unit including DFIG, RSC and GSC is modeled in detail without the addition of virtual inertia.

4.1.1.1 DFIG Modeling

DFIG behavior can be illustrated by Equations (3.1) to (3.10), if the system voltage and current remain balanced. To make a Linear Time Invariant (LTI) state space, these equations should be linearized at an equilibrium point. By considering the DFIG's currents as the system states, the DFIG can be represented as (4.1); (4.2) should also be considered to complete the DFIG modeling.

$$\begin{bmatrix} -(L_s+L_m) & 0 & L_m & 0 \\ 0 & -(L_s+L_m) & 0 & L_m \\ -L_m & 0 & (L_r+L_m) & 0 \\ 0 & -L_m & 0 & (L_r+L_m) \end{bmatrix} \frac{d}{dt} \begin{bmatrix} \Delta i_{qs} \\ \Delta i_{ds} \\ \Delta i'_{qr} \\ \Delta i'_{dr} \end{bmatrix} =$$

$$\begin{bmatrix} -R_s & -\omega_0(L_s+L_m) & 0 & \omega_0 L_m \\ \omega_0(L_s+L_m) & -R_s & -\omega_0 L_m & 0 \\ 0 & -(\omega_0-\omega_r)L_m & R'_r & (\omega_0-\omega_r)(L_r+L_m) \\ (\omega_0-\omega_r)L_m & 0 & -(\omega_0-\omega_r)(L_r+L_m) & R'_r \end{bmatrix} \begin{bmatrix} \Delta i_{qs} \\ \Delta i_{ds} \\ \Delta i'_{qr} \\ \Delta i'_{dr} \end{bmatrix} + \begin{bmatrix} 1 & 0 & 0 & 0 \\ 0 & 1 & 0 & 0 \\ 0 & 0 & 1 & 0 \\ 0 & 0 & 0 & 1 \end{bmatrix} \begin{bmatrix} \Delta v_{qs} \\ \Delta v_{ds} \\ \Delta v'_{qr} \\ \Delta v'_{dr} \end{bmatrix} - \begin{bmatrix} \Delta\psi_{ds0} & 0 \\ -\Delta\psi_{qs0} & 0 \\ \Delta\psi'_{dr0} & -\Delta\psi'_{dr0} \\ -\Delta\psi'_{dr0} & \Delta\psi'_{dr0} \end{bmatrix} \begin{bmatrix} \Delta\omega \\ \Delta\omega_r \end{bmatrix} \tag{4.1}$$

$$T_m - T_e = 2H_{DG1}\frac{d\omega_r}{dt} \tag{4.2}$$

After a few modifications and the introduction of x_{dfig}, the DFIG state-space model can be shown as (4.4) and (4.5). Details of this model can be viewed in Appendix A.

$$x_{dfig} = \begin{bmatrix} \Delta i_{qs} \\ \Delta i_{ds} \\ \Delta i'_{qr} \\ \Delta i'_{dr} \\ \Delta\omega_r \end{bmatrix} \tag{4.3}$$

$$\dot{x}_{dfig} = A_{dfig}x_{dfig} + B_{vb,dfig}\begin{bmatrix} \Delta v_{qb} \\ \Delta v_{db} \end{bmatrix} + B_{vr,dfig}\begin{bmatrix} \Delta v'_{qr} \\ \Delta v'_{dr} \end{bmatrix} + B_{w,dfig}[\Delta\omega] + B_{tm,dfig}[\Delta P_m] \tag{4.4}$$

$$\Delta P_{rsc} = C_{dfig}x_{dfig} + D_{vb,dfig}\begin{bmatrix} \Delta v_{qb} \\ \Delta v_{db} \end{bmatrix} + D_{vr,dfig}\begin{bmatrix} \Delta v'_{qr} \\ \Delta v'_{dr} \end{bmatrix} + D_{w,dfig}[\Delta\omega] + D_{tm,dfig}[\Delta P_m] \tag{4.5}$$

4.1.1.2 RSC Modeling

Ignoring virtual inertia, $T_{e\text{-}ref}$ in (3.12) could be replaced by $T_{e,OPT}$, an assumption which is valid in conventional DFIG-based wind power generators. After this replacement, $i_{d\text{-}ref}$ can be rephrased as a function of ω_r, as is shown in (4.6). The linearized form of this equation is shown in (4.7).

$$i_{dr-ref} = \frac{K_{OPT}\omega_0(L_s + L_m)}{L_m v_{ds}}\omega_r{}^2 \tag{4.6}$$

$$\Delta i_{dr-ref} = \frac{K_{OPT}\omega_0(L_s + L_m)}{L_m}(-\frac{\omega_{r0}{}^2}{V_{db0}^2}\Delta v_{db} + \frac{2\omega_{r0}}{V_{db0}}\Delta\omega_r) \tag{4.7}$$

Although $i_{q\text{-}ref}$ has two different modes, only the islanding mode of operation will be investigated here. $i_{q\text{-}ref}$ can be divided to two components: $i_{qr,mag}$ and $i_{qr,gen}$. The linearized form of $i_{qr,mag}$ is shown in (4.8).

$$\Delta i_{qr,mag-ref} = -\frac{1}{\omega_0 L_m}\Delta v_{db} \tag{4.8}$$

$i_{qr\text{-}gen}$ is responsible for regulating the magnitude of the stator voltage. This magnitude is derived from (4.9). Its linearized form is shown in (4.10).

$$v_T = \sqrt{v_{ds}^2 + v_{qs}^2} \tag{4.9}$$

$$\Delta v_T = \frac{1}{\sqrt{V_{ds0}^2 + V_{qs0}^2}}\begin{bmatrix} V_{qs0} & V_{ds0}\end{bmatrix}\begin{bmatrix}\Delta v_{qs}\\ \Delta v_{ds}\end{bmatrix} \tag{4.10}$$

v_s is an output of the DFIG state-space model and consequently can be represented as a function of the states and the inputs of the DFIG model. This representation of v_s is described in detail in Appendix A.

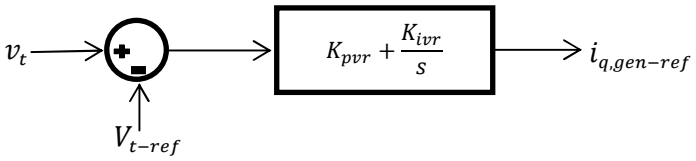

Figure 4.2 DFIG Stator Voltage Regulator

To make a state-space representation, a new state, μ_{rv}, is defined, as in (4.11). By substituting Δv_t and $\Delta v_{t\text{-}ref}$ with (4.10) and zero, respectively, (4.13) will be derived. Later, Δv_s will be also replaced by (A.11).

$$\Delta\dot{\mu}_{rv} = \Delta v_t - \Delta v_{t-ref} \tag{4.11}$$

$$\Delta i_{q,gen} = K_{ivr}[\mu_{rv}] + K_{pvr}[\Delta v_t] - K_{pvr}[\Delta v_{t-ref}] \tag{4.12}$$

$$\Delta\dot{\mu}_{rv} = [0][\mu_{rv}] + \frac{1}{\sqrt{V_{ds0}^2 + V_{qs0}^2}}\begin{bmatrix} V_{qs0} & V_{ds0}\end{bmatrix}\begin{bmatrix}\Delta v_{qs}\\ \Delta v_{ds}\end{bmatrix} \tag{4.13}$$

$$\Delta i_{q,gen-ref} = K_{ivr}[\mu_{rv}] + \frac{K_{pvr}}{\sqrt{V_{ds0}^2 + V_{qs0}^2}} \begin{bmatrix} V_{qs0} & V_{ds0} \end{bmatrix} \begin{bmatrix} \Delta v_{qs} \\ \Delta v_{ds} \end{bmatrix} \tag{4.14}$$

Now, based on (3.14), (4.8) and (4.14), $i_{q\text{-ref}}$ can be derived, as below:

$$\Delta i_{q-ref} = K_{ivr}[\mu_{rv}] + \frac{K_{pvr}}{\sqrt{V_{ds0}^2 + V_{qs0}^2}} \begin{bmatrix} V_{qs0} & V_{ds0} \end{bmatrix} \begin{bmatrix} \Delta v_{qs} \\ \Delta v_{ds} \end{bmatrix} + \begin{bmatrix} 0 & -\frac{1}{\omega_0 L_m} \end{bmatrix} \begin{bmatrix} \Delta v_{qb} \\ \Delta v_{db} \end{bmatrix} \tag{4.15}$$

To model the RSC current controller shown in Figure 3.3, two new states should be introduced. The outputs of this part are the modulation indexes fed to switches. They are defined in (4.18) and (4.19).

$$\Delta \dot{\mu}_{rq} = \Delta i_{qr} - \Delta i_{qr-ref} \tag{4.16}$$

$$\Delta \dot{\mu}_{rd} = \Delta i_{dr} - \Delta i_{dr-ref} \tag{4.17}$$

$$\Delta m_{rq} = K_{ir}\Delta \mu_{rq} - K_{pr}\Delta i_{qr} + K_{pr}\Delta i_{qr-ref} \tag{4.18}$$

$$\Delta m_{rd} = K_{ir}\Delta \mu_{rd} - K_{pr}\Delta i_{dr} + K_{pr}\Delta i_{dr-ref} \tag{4.19}$$

As mentioned previously, these modulation indexes will be used to generate the converter output voltage. Assuming an ideal convertor, the output voltage can be considered as modulation indexes multiplied by half of a DC-link voltage, as shown in (4.20). The half factor is because of the PWM and DC component, which is neutralized in three phases. The linearized form of (4.20) is shown in (4.21).

$$\begin{bmatrix} v_{qr} \\ v_{dr} \end{bmatrix} = 0.5 v_{DC} \times \begin{bmatrix} m_{qr} \\ m_{dr} \end{bmatrix} \tag{4.20}$$

$$\begin{bmatrix} \Delta v_{qr} \\ \Delta v_{dr} \end{bmatrix} = 0.5 V_{DC0} \begin{bmatrix} \Delta m_{qr} \\ \Delta m_{dr} \end{bmatrix} + \begin{bmatrix} 0.5 M_{qr0} \\ 0.5 M_{dr0} \end{bmatrix} [\Delta v_{DC}] \tag{4.21}$$

Based on these new equations, the RSC state-space model will be developed. The details of these equations are shown in Appendix B.

$$\dot{x}_{rsc} = A_{rsc}x_{rsc} + B_{dfig,rsc}x_{dfig} + B_{vs,rsc}\begin{bmatrix} \Delta v_{qs} \\ \Delta v_{ds} \end{bmatrix} + B_{vb,rsc}\begin{bmatrix} \Delta v_{qb} \\ \Delta v_{db} \end{bmatrix} + B_{vDC,rsc}[\Delta v_{DC}] \tag{4.22}$$

$$\begin{bmatrix} \Delta v'_{qr} \\ \Delta v'_{dr} \end{bmatrix} = C_{rsc}x_{rsc} + D_{dfig,rsc}x_{dfig} + D_{vs,rsc}\begin{bmatrix} \Delta v_{qs} \\ \Delta v_{ds} \end{bmatrix} + D_{vb,rsc}\begin{bmatrix} \Delta v_{qb} \\ \Delta v_{db} \end{bmatrix} + D_{vDC,rsc}[\Delta v_{DC}] \tag{4.23}$$

$$x_{rsc} = \begin{bmatrix} \Delta \mu_{rq} & \Delta \mu_{rd} & \Delta \mu_{rv} \end{bmatrix}^T \tag{4.24}$$

4.1.1.3 GSC Modeling

4.1.1.3.1 Super-capacitance connected via DC/DC converter to the DC-link

First, the method in which the Super-Capacitor is connected via a DC/DC convertor will be discussed. GSC will be modeled in a similar way to RSC. All equations will be linearized based on an equilibrium point, and a new state for each PI regulator will be introduced. For a DC-link regulator, (as shown in Figure 3.4), γ_d will be used. Since the reference voltage is usually constant, $\Delta v_{DC\text{-}ref}$ can be assumed to be zero.

$$\Delta\dot{\gamma}_{cd} = \Delta v_{DC-ref} - \Delta v_{DC} \tag{4.25}$$

$$\Delta i_{dc-ref} = K_{igd}[\gamma_{cd}] + K_{pgd}[\Delta v_{DC-ref}] - K_{pgd}[\Delta v_{DC}] \tag{4.26}$$

To model reactive power regulating shown in Figure 3.8, γ_d is defined as a new state. In this part, Q should be stated as a function of v_b and i_c and be linearized. Similar to $\Delta v_{DC\text{-}ref}$, ΔQ_{ref} could be considered zero.

$$Q = v_{qb} i_{db} - v_{db} i_{qb} \tag{4.27}$$

$$\Delta Q = \begin{bmatrix} -V_{db0} & V_{qb0} \end{bmatrix} \begin{bmatrix} \Delta i_{qc} \\ \Delta i_{dc} \end{bmatrix} + \begin{bmatrix} I_{dc0} & -I_{qc0} \end{bmatrix} \begin{bmatrix} \Delta v_{qb} \\ \Delta v_{db} \end{bmatrix} \tag{4.28}$$

$$\Delta\dot{\gamma}_{cq} = \Delta Q - \Delta Q_{ref} = \begin{bmatrix} -V_{db0} & V_{qb0} \end{bmatrix} \begin{bmatrix} \Delta i_{qc} \\ \Delta i_{dc} \end{bmatrix} + \begin{bmatrix} I_{dc0} & -I_{qc0} \end{bmatrix} \begin{bmatrix} \Delta v_{qb} \\ \Delta v_{db} \end{bmatrix} \tag{4.29}$$

$$\Delta i_{qc-ref} = K_{igq}[\gamma_{cq}] - K_{pgq}[\Delta Q_{ref}] + K_{pgd}[\Delta Q] = K_{igq}[\gamma_{cq}] + K_{pgd}\begin{bmatrix} -V_{db0} & V_{qb0} \end{bmatrix} \begin{bmatrix} \Delta i_{qc} \\ \Delta i_{dc} \end{bmatrix} + K_{pgd}\begin{bmatrix} I_{dc0} & -I_{qc0} \end{bmatrix} \begin{bmatrix} \Delta v_{qb} \\ \Delta v_{db} \end{bmatrix} \tag{4.30}$$

Two new states, φ_{cd} and φ_{cq}, will be considered to model the current regulator shown in Figure 3.10.

$$\Delta\dot{\varphi}_{cq} = \Delta i_{qc} - \Delta i_{qc-ref} \tag{4.31}$$

$$\Delta\dot{\varphi}_{cd} = \Delta i_{dc} - \Delta i_{dc-ref} \tag{4.32}$$

$$\begin{bmatrix} \Delta m_{cq} \\ \Delta m_{cd} \end{bmatrix} = \begin{bmatrix} -K_{ic} & 0 \\ 0 & -K_{ic} \end{bmatrix} \begin{bmatrix} \Delta\varphi_{cq} \\ \Delta\varphi_{cd} \end{bmatrix} + \begin{bmatrix} K_{pc} & -X_s \\ -X_s & K_{pc} \end{bmatrix} \begin{bmatrix} \Delta i_{qc} \\ \Delta i_{dc} \end{bmatrix} + \begin{bmatrix} -K_{pc} & 0 \\ 0 & -K_{pc} \end{bmatrix} \begin{bmatrix} \Delta i_{qc-ref} \\ \Delta i_{dc-ref} \end{bmatrix} \tag{4.33}$$

The relation between modulation indexes and output voltages is similar to the RSC case.

$$\begin{bmatrix} v_{qc} \\ v_{dc} \end{bmatrix} = 0.5 v_{DC} \times \begin{bmatrix} m_{qc} \\ m_{dc} \end{bmatrix} \tag{4.34}$$

$$\begin{bmatrix}\Delta v_{qc}\\ \Delta v_{dc}\end{bmatrix} = 0.5V_{DC0}\begin{bmatrix}\Delta m_{qc}\\ \Delta m_{dc}\end{bmatrix} + \begin{bmatrix}0.5M_{qc0}\\ 0.5M_{dc0}\end{bmatrix}[\Delta v_{DC}] \tag{4.35}$$

To complete this part, the reactance between the GSC and generator bus should be modeled. The schematic of this reactance is shown in Figure 3.9 and described in Equation (3.27). In these cases, R_s is assumed be negligible. The state-space representation of the reactance is illustrated below.

$$\frac{d}{dt}\begin{bmatrix}\Delta i_{cq}\\ \Delta i_{cd}\end{bmatrix} = \begin{bmatrix}0 & -\omega_0\\ \omega_0 & 0\end{bmatrix}\begin{bmatrix}\Delta i_{cd}\\ \Delta i_{cq}\end{bmatrix} + \begin{bmatrix}\frac{1}{L_s} & 0\\ 0 & \frac{1}{L_s}\end{bmatrix}\begin{bmatrix}\Delta v_{bq}\\ \Delta v_{bd}\end{bmatrix} + \begin{bmatrix}-\frac{1}{L_s} & 0\\ 0 & -\frac{1}{L_s}\end{bmatrix}\begin{bmatrix}\Delta v_{cq}\\ \Delta v_{bd}\end{bmatrix} + \frac{1}{L}\begin{bmatrix}-I_{cd0}\\ I_{cq0}\end{bmatrix}[\Delta\omega] \tag{4.36}$$

All of these equations can be summarized and represented as (4. 37) to (4. 39), and are discussed in Appendix C in detail.

$$\dot{x}_{gsc} = A_{gsc}x_{gsc} + B_{vb,gsc}\begin{bmatrix}\Delta v_{qb}\\ \Delta v_{db}\end{bmatrix} + B_{vDC,gsc}[\Delta v_{DC}] + B_{\omega,gsc}[\Delta\omega] \tag{4.37}$$

$$\Delta P_{gsc} = C_{gsc}x_{gsc} + D_{vb,gsc}\begin{bmatrix}\Delta v_{qb}\\ \Delta v_{db}\end{bmatrix} + D_{vDC,gsc}[\Delta v_{DC}] + D_{w,gsc}[\Delta\omega] \tag{4.38}$$

$$x_{gsc} = \begin{bmatrix}\Delta\gamma_{cq} & \Delta\gamma_{cd} & \Delta\varphi_{cq} & \Delta\varphi_{cd} & \Delta i_{cq} & \Delta i_{cd}\end{bmatrix}^T \tag{4.39}$$

4.1.1.3.2 Super-capacitance connected directly to the DC-link

The major difference is in active power regulation. For this topology, the active power regulation in Figure 3.7 and 3.8 should be modeled. In Figure 3.7, the DC-link regulating block does not usually incorporate in setting the reference power and is zero except in rare stream cases, so this part could be ignored. $\tilde{P}r$, which is introduced as a measurement of RSC power, could be represented as below.

$$\tilde{P}_r = \frac{\omega_f}{s+\omega_f}P_{rsc} \tag{4.40}$$

Based on Figure 3.7 and (4.40), the first part of power controller could be modeled as (4.41). In this equation, a new parameter ϕ_1 is used to make the modeling possible.

$$\Delta\dot{\phi}_1 = [\omega_f][\Delta\phi_1] + [1][\Delta P_{rsc}] + [0][\Delta P_{vi}] \tag{4.41}$$

$$\Delta P_{ref} = [\omega_f][\Delta\phi_1] + [0][\Delta P_{rsc}] + [1][\Delta P_{vi}] \tag{4.42}$$

The output of this part will be used as an input for an active power regulating block shown in Figure 3.8. It will be modeled similar to a DC-link voltage regulator or reactive power regulator, as

discussed above, and a new parameter ϕ_2 will be used. P_{gsc} can also be represented as (4.45). The linearized form is shown in (4.46).

$$\Delta\dot{\phi}_2 = \Delta P_{ref} - \Delta P_{gsc} \tag{4.43}$$

$$\Delta i_{dc-ref} = K_{igd}\left[\phi_2\right] - K_{pgd}\left[\Delta P_{ref}\right] + K_{pgd}\left[\Delta P_{gsc}\right] \tag{4.44}$$

$$P_{gsc} = v_{db} i_{db} + v_{qb} i_{qb} \tag{4.45}$$

$$\Delta P_{gsc} = \begin{bmatrix} V_{qb0} & V_{db0} \end{bmatrix} \begin{bmatrix} \Delta i_{qc} \\ \Delta i_{dc} \end{bmatrix} + \begin{bmatrix} I_{qc0} & I_{dc0} \end{bmatrix} \begin{bmatrix} \Delta v_{qb} \\ \Delta v_{db} \end{bmatrix} \tag{4.46}$$

(4.43) and (4.44) also can be rephrased as (4.47) and (4.48).

$$\Delta\dot{\phi}_2 = [0][\phi_2] + \left[\Delta P_{ref}\right] + \begin{bmatrix} -V_{qb0} & -V_{db0} \end{bmatrix} \begin{bmatrix} \Delta i_{qc} \\ \Delta i_{dc} \end{bmatrix} + \begin{bmatrix} -I_{qc0} & -I_{dc0} \end{bmatrix} \begin{bmatrix} \Delta v_{qb} \\ \Delta v_{db} \end{bmatrix} \tag{4.47}$$

$$\Delta i_{dc-ref} = K_{igd}\left[\phi_2\right] - K_{pgd}\left[\Delta P_{ref}\right] + K_{igd}\begin{bmatrix} V_{qb0} & V_{db0} \end{bmatrix} \begin{bmatrix} \Delta i_{qc} \\ \Delta i_{dc} \end{bmatrix} + K_{pgd}\begin{bmatrix} I_{qc0} & I_{dc0} \end{bmatrix} \begin{bmatrix} \Delta v_{qb} \\ \Delta v_{db} \end{bmatrix} \tag{4.48}$$

The rest of controller is exactly the same as the former case, so the x_{gsc} should be modified to (4.49). The details of state-space are shown in Appendix C.

$$x_{gsc} = \begin{bmatrix} \Delta\gamma_{cq} & \Delta\phi_1 & \Delta\phi_2 & \Delta\varphi_{cq} & \Delta\varphi_{cd} & \Delta i_{cq} & \Delta i_{cd} \end{bmatrix}^T \tag{4.49}$$

4.1.1.4 DC-Link Modeling

Equation (3.22), which explains the DC-link behavior, will be linearized and rephrased as (4.50). In cases involving the direct connection of the Super-Capacitor to the DC-link, C_{scap} should be used instead of $C_{dc\text{-}link}$.

$$\Delta\dot{v}_{DC} = [0][\Delta v_{DC}] + \frac{1}{C_{dc-link} V_{DC0}}\left[\Delta P_{rsc}\right] - \frac{1}{C_{dc-link} V_{DC0}}\left[\Delta P_{gsc}\right] \tag{4.50}$$

The model derived here can be combined to make the wind power plant model. The wind power state-space model is shown in (4.51) to (4.54).

$$x_{wind} = \begin{bmatrix} \Delta x_{dfig}^T & \Delta x_{rsc}^T & \Delta x_{gsc}^T & \Delta v_{DC} \end{bmatrix}^T \tag{4.51}$$

$$A_{wind} = \begin{bmatrix} A_{dfig} + B_{vr,dfig}(D_{dfig,rsc} + D_{vs,rsc}F_{dfig}) & B_{vr,dfig}C_{rsc} & 0 & B_{vr,dfig}D_{vDC,rsc} \\ B_{dfig,rsc} + B_{vs,rsc}F_{dfig} & A_{rsc} & 0 & B_{vDC,rsc} \\ B_{pr,gsc}C_{dfig} & B_{pr,gsc}D_{vr,dfig}C_{rsc} & A_{gsc} & B_{vDC,gsc} \\ \frac{1}{C_{dc-link}V_{DC0}}(C_{dfig} + D_{vr,dfig}D_{vs,rsc}F_{dfig}) & \frac{1}{C_{dc-link}V_{DC0}}D_{vr,dfig}C_{rsc} & -\frac{1}{C_{dc-link}V_{DC0}}C_{gsc} & 0 \end{bmatrix} \tag{4.52}$$

$$B_{vb,wind} = \begin{bmatrix} B_{vb,dfig} + B_{vr,dfig}(D_{vb,rsc} + D_{vs,rsc}F_{vb}) \\ B_{vb,rsc} + B_{vs,rsc}F_{vb} \\ B_{vb,gsc} + B_{pr,gsc}(D_{vb,dfig} + D_{vr,dfig}(D_{vb,rsc} + D_{vs,rsc}F_{vb})) \\ -\frac{1}{C_{dc-link}V_{DC0}}D_{vb,gsc} \end{bmatrix},$$

$$B_{\omega,wind} = \begin{bmatrix} B_{\omega,dfig} + B_{vr,dfig}D_{vs,rsc}F_{\omega} \\ B_{vs,rsc}F_{\omega} \\ B_{\omega,gsc} + B_{pr,gsc}(D_{\omega,dfig} + D_{vr,dfig}D_{vs,rsc}F_{\omega})) \\ -\frac{1}{C_{dc-link}V_{DC0}}D_{\omega,gsc} \end{bmatrix}, \quad B_{tm,wind} = \begin{bmatrix} B_{tm,dfig} + B_{vr,dfig}D_{vs,rsc}F_{tm}) \\ B_{vs,rsc}F_{tm} \\ [0]_{6\times 1} \\ 0 \end{bmatrix} \tag{4.53}$$

$$\dot{x}_{wind} = A_{wind}x_{wind} + B_{vb,wind}\begin{bmatrix} \Delta v_{qb} \\ \Delta v_{db} \end{bmatrix} + +B_{w,wind}[\Delta\omega] + B_{tm,wind}[\Delta T_m] \tag{4.54}$$

4.1.2 Simplified Model

Table 1 shows the eigen-values of the complete DG1 model, the wind power generator without virtual inertia, and the Super-Capacitor. It consists of 15 states. The detailed model of the microgrid, which includes two DG units, 6 loads and several lines, is much more complicated. In the simplified form, DG1 has one dominant pole far from the other modes. This situation may lead to simplifying DG1 as a first order system. However, prior to doing this, we need to know which state this mode belongs to.

Table 4.1 DG1 Complete Model Eigen-Values

λ_1	-7.05E+04
λ_2	-8.25E+04
λ_3	-4.14E+03
λ_4	-5.74E+02
$\lambda_{5,6}$	-20.046 ± j367.266
$\lambda_{7,8}$	-70.515 ± j302.879
$\lambda_{9,10}$	-49.550 ± j230.454
λ_{11}	-0.6676
λ_{12}	-38.3635
λ_{13}	-43.7177
λ_{14}	-50.2413
λ_{15}	-50.0004

Participation factor analysis, Table 4.2, shows that the modes λ_5 to λ_{12} are impacted by DFIG, RSC and its controller while the rest of the modes are more related to the DC-link, GSC and its controller.

In particular, λ_{11} is influenced by ω_r, the rotational speed of DFIG. The sensitivity analysis, Table 4.3, reveals that the effect of elements of A_{wind} which contains H_{DG1}, the moment of inertia of the DFIG rotating mass, on this mode is significant. On the other hand, the only equation which contains this factor is (4.53), which is a representation of (2.9) in per-unit scale.

$$P_m - P_e = 2H_{DG1}\omega_r \frac{d\omega_r}{dt} \tag{4.53}$$

Since the controller is designed to maximize wind power extraction, in an equilibrium point, as shown in Figure 2.3, $\partial P_m/\partial \omega_r$ is zero. In addition, P_e can be replaced by P_{OPT} in (3.17). After these replacements and the linearization needed for small signal analysis, (4.53) can be rephrased as (4.54).

$$\Delta P_m - 3K_{OPT}\omega_{r0}{}^2\Delta\omega_r = 2H_{DG1}\omega_{r0}\frac{d\Delta\omega_r}{dt} \tag{4.54}$$

Obviously, the mode derived from this equation depends on ω_{r0}, which is the DFIG initial rotational speed. Figure 4.3 shows the dominant pole of the detailed model and the derived pole of equation (4.54) versus ω_{r0}, plus their high coincidence. In other words, the controllers are fast enough to assume that P_e equals P_{opt} and to use (4.54) as a representation of the whole wind power generator.

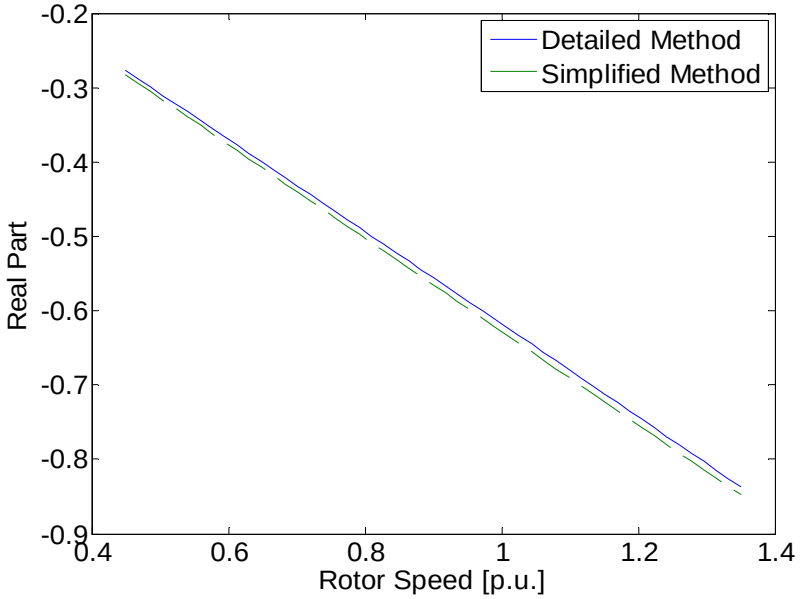

Figure 4.3 the Dominant Pole of the Detailed Model and the Simplified Model Pole versus DFIG Rotational Speed

It should be mentioned here that in cases involving the direct connection of the Super-Capacitor to the DC-link, the same patterns in eigen-value analysis will be obtained.

Table 4.2 Participation Factor Analysis Result

	λ_1	λ_2	λ_3	λ_4	λ_5	λ_6	λ_7	λ_8	λ_9	λ_{10}	λ_{11}	λ_{12}	λ_{13}	λ_{14}	λ_{15}
Δi_{qs}	1E-09	3E-14	7 E-07	2.1E-04	9.28	9.28	5.11	5.11	5.48	5.48	5E-06	2E-01	5E-09	7E-08	1E-07
Δi_{ds}	4E-11	1E-15	4E-06	3.6E-04	11.38	11.38	1.18	1.18	9.97	9.97	2.8E-03	4.6E-04	5.2E-10	3.2E-08	4.7E-08
$\Delta i'_{qr}$	1.7E-09	3.9E-14	1.2E-07	2.1E-04	8.85	8.85	5.47	5.47	5.52	5.52	9.5E-06	2.5E-01	6.1E-09	8.5E-08	1.2E-07
$\Delta i'_{dr}$	6.8E-09	1.5E-13	3.8E-05	5.1E-05	10.88	10.88	1.21	1.21	10.43	10.43	2.8E-03	1.9E-03	5.6E-10	3.5E-08	5.2E-08
$\Delta \omega_r$	5.6E-15	1.1E-19	1.4E-09	2.3E-07	2.1E-04	2.1E-04	3.4E-04	3.4E-04	0.0045	0.0045	0.99	6.0E-06	1.0E-11	4.9E-10	7.3E-10
$\Delta \mu_{rq}$	3.4E-12	6.6E-17	2.8E-07	6.5E-06	0.024	0.024	0.493	0.493	0.075	0.075	1.0E-07	6.1E-02	4.3E-10	2.3E-09	3.7E-09
$\Delta \mu_{rd}$	2.2E-11	4.2E-16	2.1E-06	1.3E-4	0.011	0.011	0.049	0.049	0.474	0.474	0.008	2.3E-03	1.4E-10	9.7E-09	1.4E-08
$\Delta \mu_{rv}$	2.6E-13	5.0E-18	1.7E-08	3.3E-09	1.9E-03	1.9E-03	6.2E-02	6.2E-02	3.9E-03	3.9E-03	8.0E-08	1.04	9.5E-09	8.5E-08	1.3E-07
$\Delta \gamma_{cq}$	3.1E-08	5.3E-04	1.4E-08	1.7E-08	1.2E-12	1.2E-12	5.6E-12	5.6E-12	2.0E-11	2.0E-11	3.9E-20	1.8E-09	9.6E-01	3.2E-02	3.0E-08
$\Delta \gamma_{cd}$	5.1E-04	1.3E-08	1.7E-01	1.17	9.5E-06	9.5E-06	3.8E-05	3.8E-05	1.0E-04	1.0E-04	1.6E-09	3.6E-06	5.1E-08	2.4E-06	1.1E-05
$\Delta \varphi_{cq}$	3.5E-08	6.1E-4	1.6E-08	2.0E-08	1.4E-12	1.4E-12	6.4E-12	6.4E-12	2.3E-11	2.3E-11	6.9E-18	1.0E-09	0.028	0.972	4.4E-04
$\Delta \varphi_{cd}$	7.6E-04	2.3E-08	8.9E-04	1.4E-04	7.6E-09	7.6E-09	2.7E-08	2.7E-08	7.4E-08	7.4E-08	2.0E-16	2.3E-08	3.7E-07	4.4E-04	1.0
Δi_{cq}	4.2E-05	1	7.0E-08	1.7E-09	4.6E-14	4.6E-14	1.5E-13	1.5E-13	3.1E-13	3.1E-13	7.3E-25	2.5E-12	3.5E-03	4.7E-03	2.1E-06
Δi_{cd}	1.07	4.44	0.0733	1.4E-03	5.6E-08	5.6E-08	1.6E-07	1.6E-07	3.4E-07	3.4E-07	2.0E-16	5.6E-09	1.7E-13	3.7E-10	8.2E-07
Δv_{DC}	0.0716	2.2E-06	1.243	0.171	5.8E-07	5.8E-07	1.6E-06	1.6E-06	2.6E-06	2.6E-06	3.3E-16	2.4E-09	3.9E-08	1.8E-06	2.6E-06

Table 4.3 Sensitivity Analysis Result; the highlighted cells refer to corresponding elements in A_{wind}, $-L_mI_{qr0}/2H_{DG1}$, $-L_mI_{qs0}/2H_{DG1}$, $-K_{OPT}/H_{DG1}$.

5.86E-06	0.001157	1.00E-05	0.001218	0.000847	8.41E-06	2.30E-05	4.45E-09	1.87E-10	1.37E-05	1.38E-08	1.22E-10	1.30E-10	0.000686	9.18E-06
1.43E-05	0.002814	2.44E-05	0.002964	0.00206	2.05E-05	5.59E-05	1.08E-08	4.56E-10	3.34E-05	3.36E-08	2.97E-10	3.17E-10	0.00167	2.23E-05
5.57E-06	0.001098	9.52E-06	0.001156	0.000804	7.98E-06	2.18E-05	4.22E-09	1.78E-10	1.30E-05	1.31E-08	1.16E-10	1.24E-10	0.000652	8.71E-06
1.35E-05	0.00267	2.32E-05	0.002813	0.001955	1.94E-05	5.31E-05	1.03E-08	4.33E-10	3.17E-05	3.19E-08	2.82E-10	3.00E-10	0.001585	2.12E-05
0.00687	1.35482	0.011752	1.427047	0.991735	0.009852	0.026926	5.21E-06	2.20E-07	0.016102	1.62E-05	1.43E-07	1.52E-07	0.80404	0.01075
7.06E-08	1.39E-05	1.21E-07	1.47E-05	1.02E-05	1.01E-07	2.77E-07	5.36E-11	2.26E-12	1.66E-07	1.67E-10	1.47E-12	1.57E-12	8.27E-06	1.11E-07
0.002109	0.415943	0.003608	0.438117	0.304473	0.003025	0.008266	1.60E-06	6.74E-08	0.004944	4.97E-06	4.40E-08	4.68E-08	0.246848	0.0033
0.000106	0.020864	0.000181	0.021976	0.015272	0.000152	0.000415	8.02E-08	3.38E-09	0.000248	2.49E-07	2.21E-09	2.35E-09	0.012382	0.000166
1.23E-15	2.43E-13	2.11E-15	2.56E-13	1.78E-13	1.77E-15	4.83E-15	9.35E-19	3.94E-20	2.89E-15	2.91E-18	2.57E-20	2.74E-20	1.44E-13	1.93E-15
7.11E-10	1.40E-07	1.22E-09	1.48E-07	1.03E-07	1.02E-09	2.79E-09	5.39E-13	2.27E-14	1.67E-09	1.68E-12	1.48E-14	1.58E-14	8.32E-08	1.11E-09
2.94E-15	5.80E-13	5.03E-15	6.10E-13	4.24E-13	4.21E-15	1.15E-14	2.23E-18	9.40E-20	6.89E-15	6.93E-18	6.13E-20	6.52E-20	3.44E-13	4.60E-15
9.61E-12	1.90E-09	1.64E-11	2.00E-09	1.39E-09	1.38E-11	3.77E-11	7.29E-15	3.07E-16	2.25E-11	2.27E-14	2.00E-16	2.13E-16	1.13E-09	1.50E-11
3.33E-20	6.56E-18	5.69E-20	6.91E-18	4.80E-18	4.77E-20	1.30E-19	2.52E-23	1.06E-24	7.80E-20	7.84E-23	6.93E-25	7.38E-25	3.89E-18	5.21E-20
1.70E-18	3.36E-16	2.91E-18	3.54E-16	2.46E-16	2.44E-18	6.68E-18	1.29E-21	5.44E-23	3.99E-18	4.02E-21	3.55E-23	3.78E-23	1.99E-16	2.67E-18
2.13E-16	4.20E-14	3.64E-16	4.43E-14	3.08E-14	3.06E-16	8.35E-16	1.62E-19	6.81E-21	4.99E-16	5.02E-19	4.44E-21	4.73E-21	2.49E-14	3.33E-16

4.1.2.1 Rotating-Mass Based Virtual Inertia

A simplified model can now be derived and studied. Based on (3.21), ΔP_e, which is a linearized form of the electrical output of DG1, can be represented as (4.55). The term $3K_{OPT}\omega_{r0}^2\Delta\omega_r$ in (4.53) should be replaced by this relation. In this new relation, $\Delta\omega_r$ and consequently ΔP_e can be found as a function of ΔP_m and $\Delta\omega_m$, as shown in (4.56) and (4.57). It should be mentioned here that DG1 representation without virtual inertia can be easily obtained by setting J_V and, as a result, H_V to zero.

$$\Delta P_e = 3K_{OPT}\omega_{r0}^{\ 2}\Delta\omega_r - H_V(s)\omega_{r0}\Delta\omega_m \tag{4.55}$$

$$\Delta\omega_r = \frac{1}{2H_{DG1}\omega_{r0}s + 3K_{OPT}\omega_{r0}^{\ 2}}\Delta P_m + \frac{H_V(s)}{2H_{DG1}s + 3K_{OPT}\omega_{r0}}\Delta\omega_m \tag{4.56}$$

$$\Delta P_e = \frac{3K_{OPT}\omega_{r0}}{2H_{DG1}s + 3K_{OPT}\omega_{r0}}\Delta P_m - \frac{2H_{DG1}H_V(s)s}{2H_{DG1}s + 3K_{OPT}\omega_{r0}}\Delta\omega_m \tag{4.57}$$

4.1.2.2 Super-Capacitor Based Virtual inertia

Based on the aforementioned discussion, the GSC controller is fast enough to be assumed ideal. Thus, the assumptions made to conclude (3.24) were reasonable. Moreover, in similar procedures, it can be shown that a DC/DC converter connected to the Super-Capacitor and its controller can be set such that (3.26) is sufficiently accurate. After these simplifications, P_{dg1} can be represented as (4.58).

$$\Delta P_{dg1} = \frac{3K_{OPT}\omega_{r0}}{2H_{DG1}s + 3K_{OPT}\omega_{r0}}\Delta P_{wind} - H_V(s)\Delta\omega_m \tag{4.58}$$

4.1.2.2.1 DC/DC convertor Modeling

This study is neither necessary nor even possible for a topology in which a Super-Capacitor is directly connected to a DC-link. However, for the other topology, it seems prudent to prove that a DC/DC converter is sufficiently fast. To that end, the controller is shown in Figure 3.5 and the circuit is modeled here. The overall model is shown in Figure 4.4.

In this modeling, regardless of how P_{ref} is generated, the DC/DC convertor and its circuit will be examined in light of how fast and accurate they are. Some assumptions have been made to simplify this modeling. For instance, switches are considered ideal as they generate the input voltage exactly and immediately. This assumption allows us to model the convertor as a controllable voltage source. The Super-Capacitor is also modeled as a capacitor in a series with a resistance called as Equivalent Series Resistance (ESR).

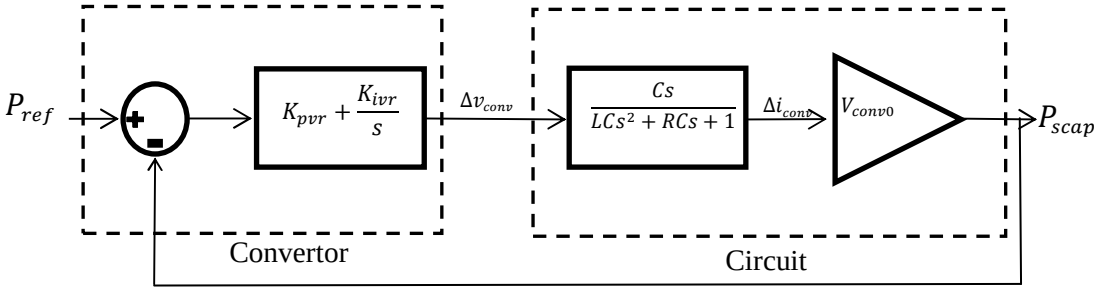

Figure 4.4 The DC/DC Block Diagram

The other assumption is about linearizing the P_{ref}; (4.59) shows its linearized form. Since the small-signal technique is used, it is linearized on an equilibrium point. In the equilibrium condition, the system frequency is constant, so the virtual inertia and consequently P_{ref} are zero, which leads to zero I_{conv0}. By considering the initial super-capacitor current zero, ΔP_{ref} can be represented by only the second term of the right-hand side of the equation:

$$\Delta P_{ref} = I_{conv0}\Delta v_{conv} + V_{conv0}\Delta i_{conv} \tag{4.59}$$

Table 4.4 shows the eigen-values of the system, and Figure 4.5 shows the response to a step input. We can clearly see that the system is indeed fast and accurate enough to be modeled as (4.58).

Table 4.4 DC/DC converter circuit eigen-values

λ_1	-1189.4
λ_2	-20.6

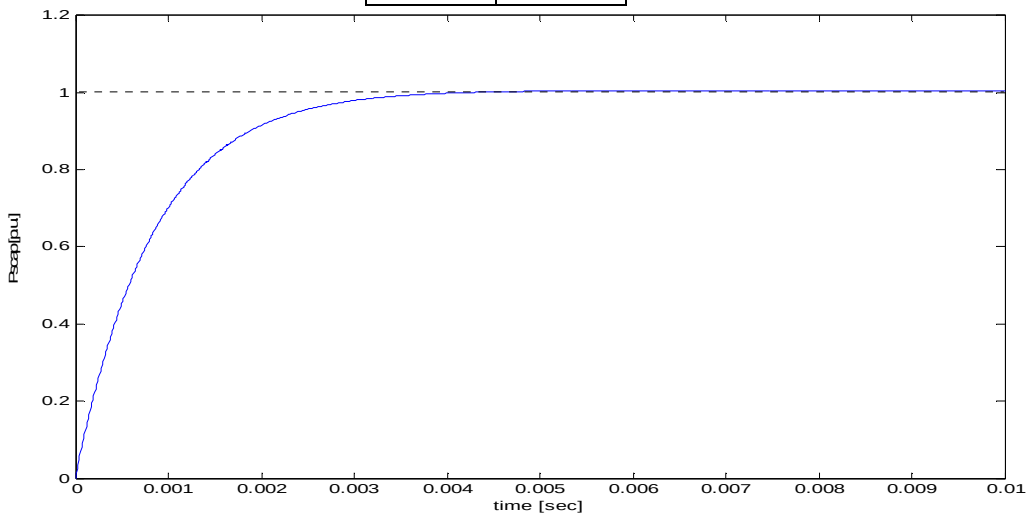

Figure 4.5 DC/DC Converter Step Response

4.2 Impact on system stability

The rest of the system, consisting of a synchronous machine, its prime mover, governor and the system loads, will be modeled as a simplified model, as discussed in [44]. The block diagram of the whole system while virtual inertia is implemented in Rotating-Mass is shown in Figure 4.6.

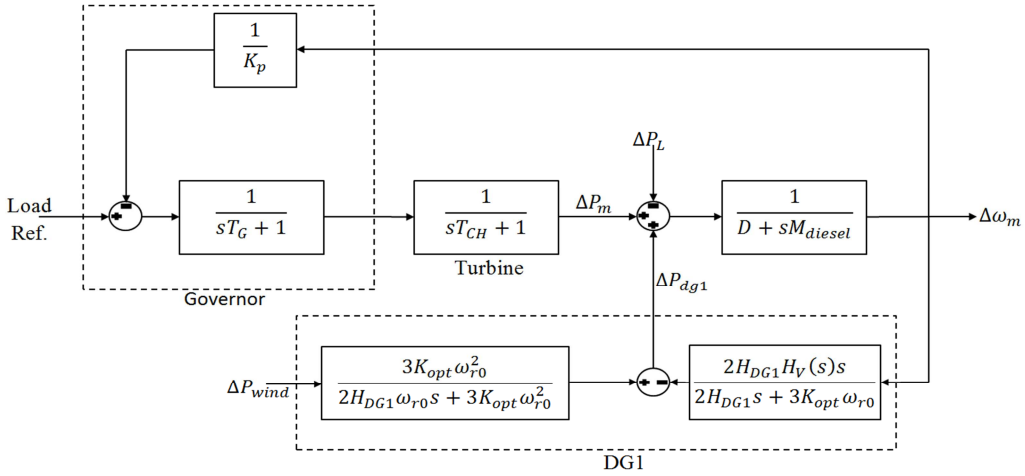

Figure 4.6 Microgrid Schematic block with a Rotating-Mass-based Virtual Inertia

4.2.1 Rotating-Mass based Virtual Inertia

Figure 4.7 shows the microgrid dominant poles root-locus by increasing J_V from zero. Virtual inertia improves system stability, but this impact is measured on a specific ω_{r0}, while in a wind power generator this value is constantly changing and therefore unpredictable.

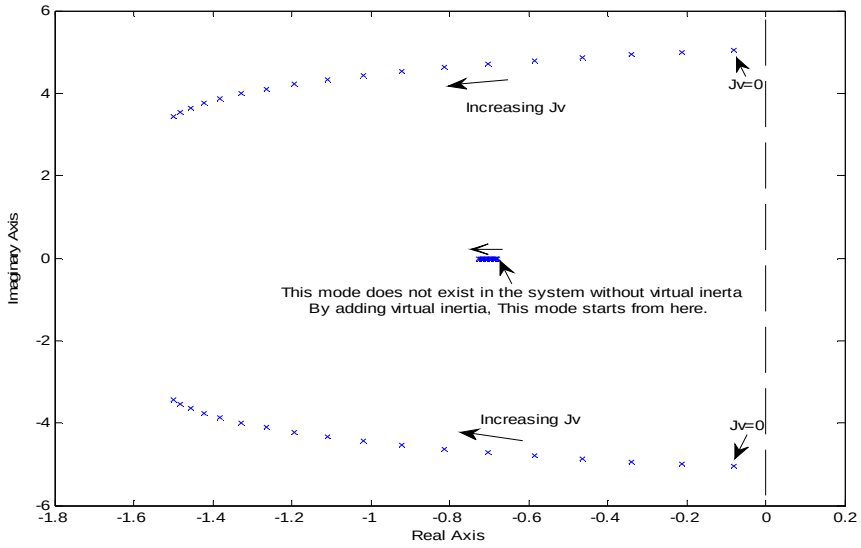

Figure 4.7 The Microgrid dominant poles Root-Locus with DFIG rotating-mass-based virtual inertia

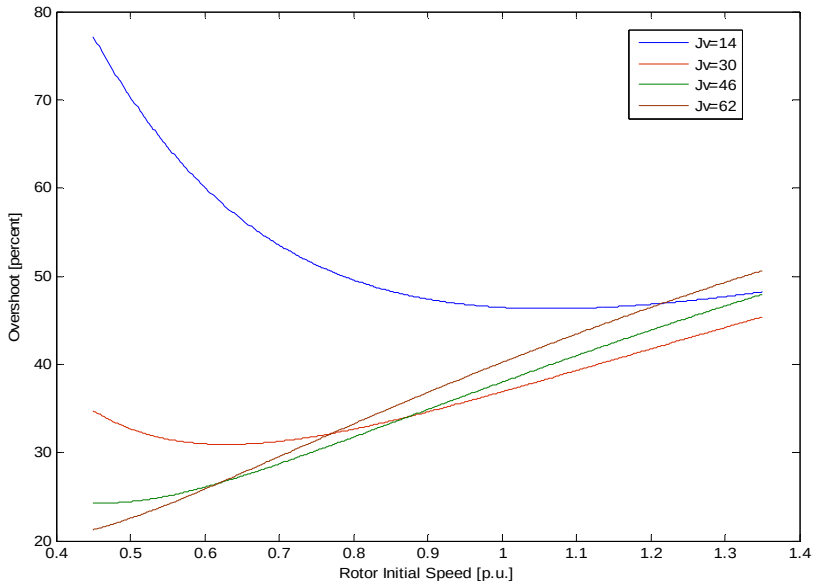

Figure 4.8 The frequency overshoots to a step change in the load, without virtual inertia vs. DFIG Rotor Initial Speed.

Figure 4.8 shows the frequency response overshoot in the presence of rotating-mass-based virtual inertia versus ω_{r0} while a step per-unit change occurs at loads. This step change can be interpreted as a mismatch between loads and generation, which takes place at the moment of intentional islanding. The frequency overshoot changes, but without virtual inertia, the amount is constant (almost 240 percent). This variation is reasonable, since different ω_{r0} means different amount of energy is stored at the DFIG rotating mass. Initial rotational speed is related to wind speed and independent of system frequency.

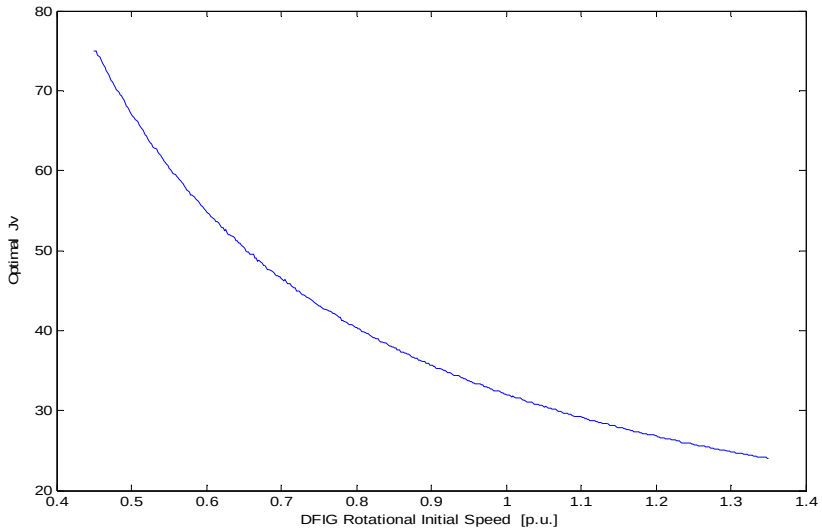

Figure 4.9 Optimal J_V vs. Initial Rotational Speed

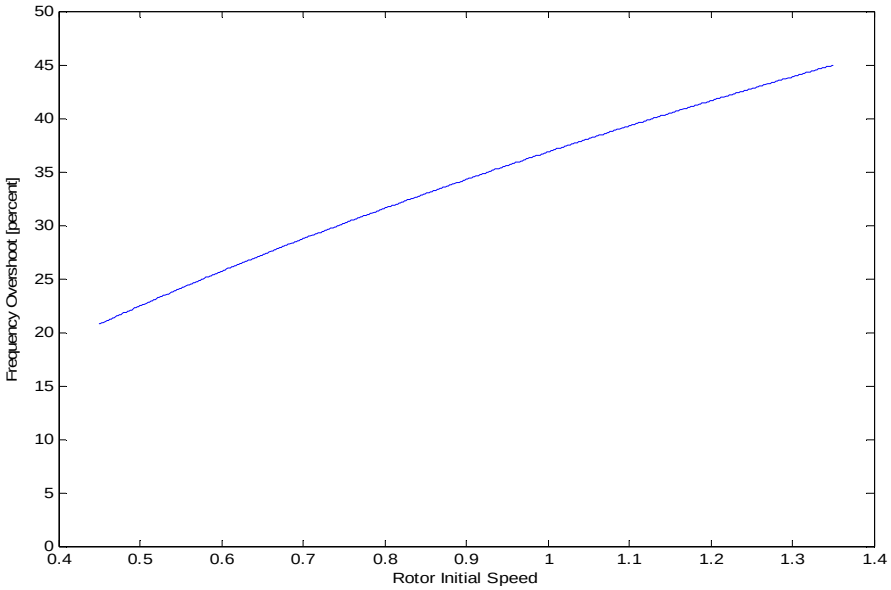

Figure 4.10 Minimum possible frequency overshoot to a step change in load in the presence of rotating-mass-based virtual inertia vs. Initial Rotational Speed

Such a dependence on the ω_{r0} may be assumed as the most disadvantageous point about using the DFIG rotating mass as the source of virtual inertia. This impact becomes more significant when ω_{r0} is zero. In this condition, virtual inertia cannot be implemented because no stored energy exists in the rotating mass. It happens when the wind speed is beyond its cut-in or cut-off speeds and is very common in the most of the systems.

Figure 4.9 depicts the optimized value of J_V versus ω_{r0} for this particular system to minimize the frequency overshoot. In Figure 4.10, the frequency response overshoots relevant to J_V described in Figure 4.9 are depicted. The inverse variation of optimal virtual inertia in respect to initial DFIG rotational speed is because of different energy stored in the rotating mass. In the other word, in lower speeds, the same changes in the rotational speed result in lower changes in power output. So to provide same power in lower speeds, more changes and consequently more virtual inertia is needed. This fact is reflected in (4.55) by the presence of ω_{r0} in the virtual inertia term of output power and could be verified by the almost constant product of optimal virtual inertia and $\omega_{r0.}$

As shown, even in the case of optimized virtual inertia, a constant frequency overshoot cannot be obtained. The other important point is the noticeably high variation in J_V. In other words, a J_V which is optimal for a specific initial rotational speed may result in a non-optimized amount in another wind speed. Considering the intermittent nature of wind, this may lead to some difficulties for designers.

4.2.2 Super-Capacitor Based virtual Inertia

Similar to the previous case, the block diagram of whole system when super-capacitor based virtual inertia is employed can be made as Figure 4.11. Figure 4.12 shows the root locus of the microgrid dominant poles where J_V is increasing. The system without virtual inertia is introduced by J_V=0. It appears to be more effective than virtual inertia using a DFIG rotating mass.

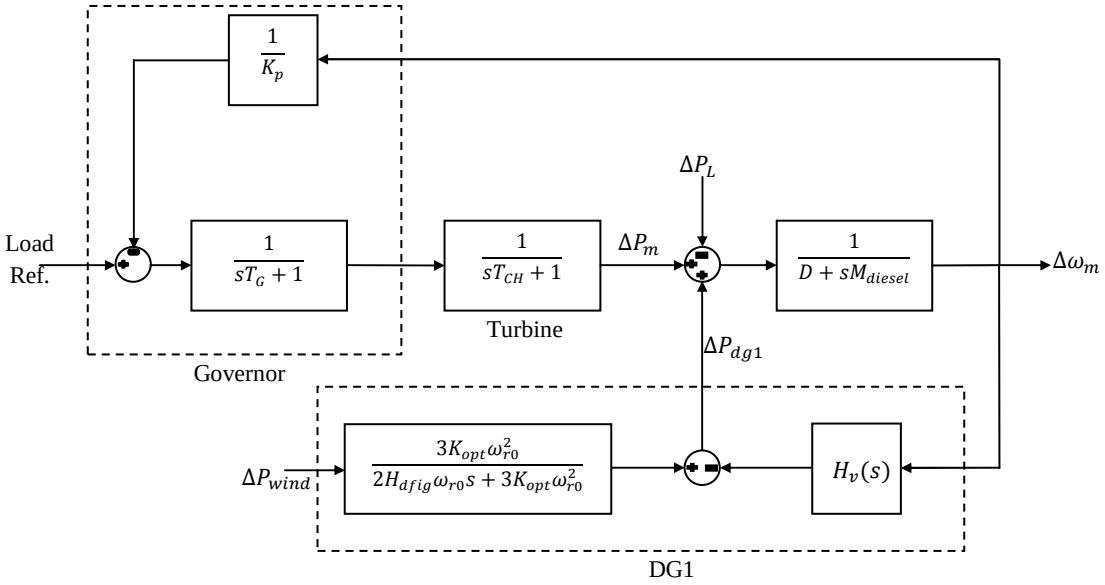

Figure 4.11 Microgrid Schematic block with a Super-Capacitor-based Virtual Inertia

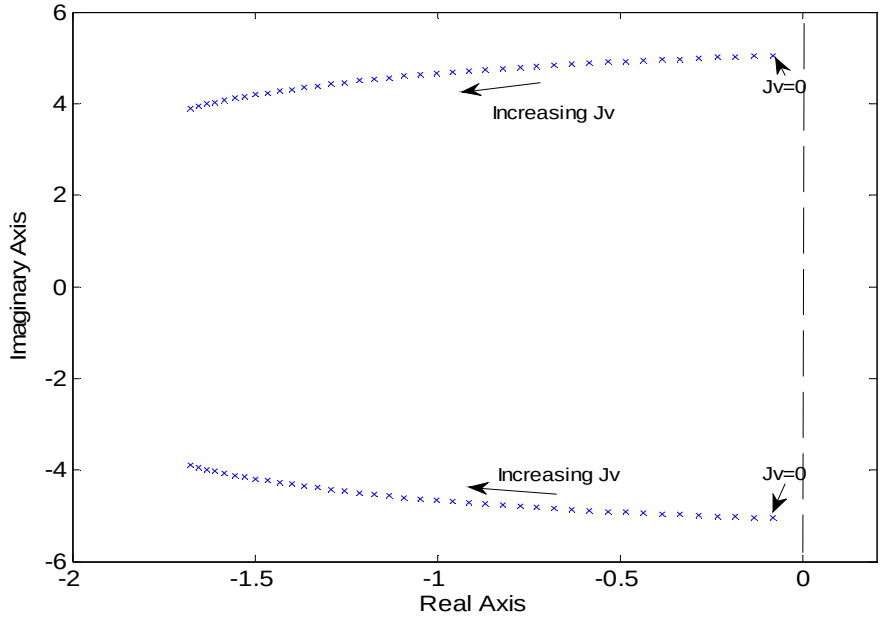

Figure 4.12 the Microgrid dominant poles' Root-Locus with Super-Capacitor based virtual inertia

The better performance of this method is clear in Figure 4.13, in which frequency response overshoots in the presence of virtual inertia in both sources versus ω_{r0} are depicted, while a step per-unit change occurs at loads. In addition, the behavior of Super-Capacitor-based virtual inertia is not dependent on the DFIG initial rotating speed. This independence, especially considering that ω_{r0} is related to unpredictable wind speed and independent of system frequency, can be assumed as an important advantage of using a Super-Capacitor instead of a DFIG rotating mass.

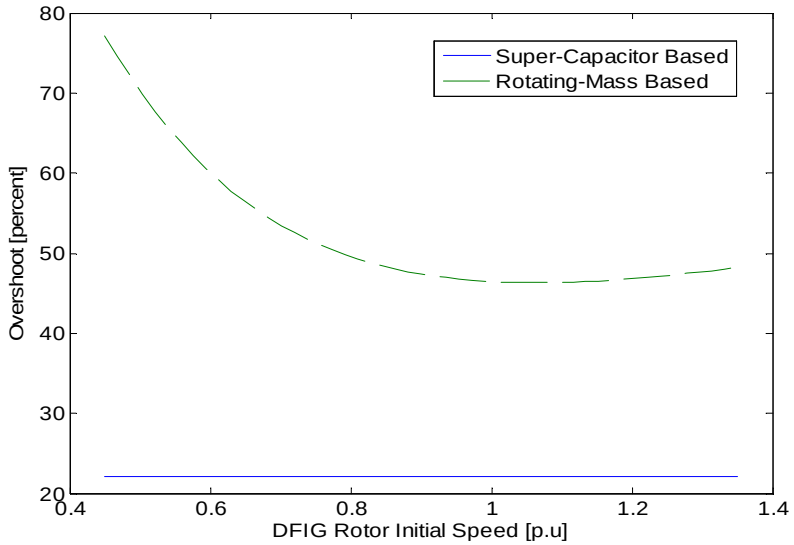

Figure 4.13 The frequency response overshoot to step change in the load vs. DFIG Rotor Initial Speed. J_V is constant, 14sec for both cases.

4.2.2.1 Sizing Super-Capacitor

The Super-Capacitor needs to be sized accurately to prevent any conflicts. By ignoring the Super-Capacitor ESR, switching losses and consequently assuming that the whole generated power is supplied by the Super-Capacitor, (4.60) can be concluded:

$$P_{scap} = \frac{1}{2} C_{scap} \frac{d(V_{scap}{}^2)}{dt} \tag{4.60}$$

On the other hand, P_{scap} can be replaced by $H_V(s)\omega_0\omega_m$ according to (3.24). As explained, $H_V(s)$ is a practical form of a derivative, so it seems reasonable to revert to the derivative form to estimate the virtual inertia power. After some calculations, (4.60) can be rephrased as (4.61).

$$\Delta V_{scap} = \frac{J_V \omega_0}{C V_0} \Delta \omega_m \tag{4.61}$$

Thus, the maximum change in the Super-Capacitor voltage, which must be controlled to prevent any over- or under-voltage, is dependent on the Super-Capacitor capacitance, J_V and the maximum frequency deviation. Meanwhile, this maximum frequency deviation is impacted by the maximum frequency overshoot, which is a function of J_V. Figure 4.14 shows this relation.

The DC/DC convertor connected to the Super-Capacitor should also be appropriately sized. Fig. 4.14 also depicts the peak power generated by the Super-Capacitor when a step change in load takes place. As mentioned, this step change can be caused by an intentional islanding. Peak output power should be used in the design of the DC/DC convertor.

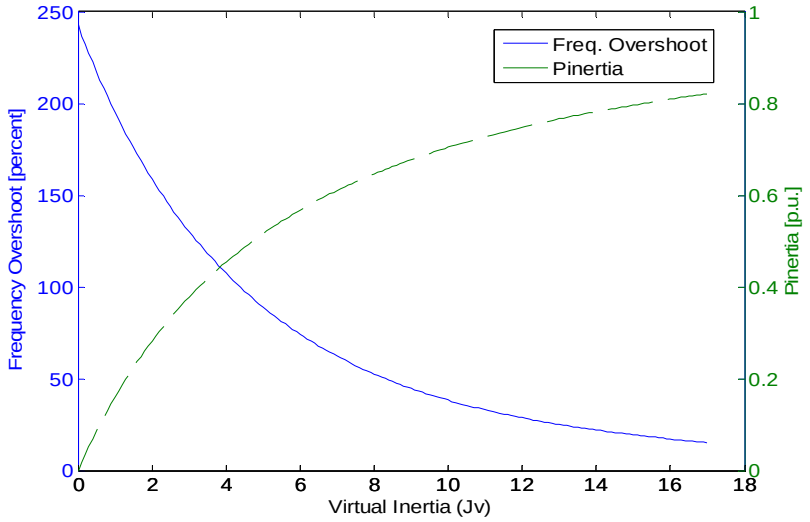

Figure 4.14 The Frequency Overshoot and the maximum power generated by a Super-capacitor when 1 p.u. change occurs in load vs Virtual Inertia when the Super-Capacitor is the source..

The situation is actually more complicated, since this power passes through the GSC. In other words, we also need to resize this part. In practice, the maximum instantaneous mismatch that could occur, usually by islanding or load disconnection, should be considered to find the final frequency. J_V can be chosen based on this final frequency and Figure 4.14 to assure the designer that the frequency always remains in the allowed range. Now, based on the other curve in Figure 4.14, the selected J_V and the maximum power mismatch, the maximum power generated by the Super-capacitor can be calculated. The value may be added to the rating of the conventional GSC, but this method is very conservative. It has been assumed that when the mismatch happens, the GSC works at its rating and also in the same direction as the maximum virtual inertia power.

The Super-Capacitor capacitance can be chosen based on (4.61), the calculated maximum frequency deviation and the allowed voltage range of the capacitor.

Here, an important disadvantage of connecting the Super-capacitor directly to the DC-link should be discussed. In this case, V_{scap} is actually $V_{dc\text{-}link}$, so controlling the V_{scap} is important, especially considering that RSC is also using this source to generate the output voltage. To reduce the DC-link fluctuations, either J_V should be decreased or the capacitance of C_{scap} should be increased. While the former solution results in a lower impact of the virtual inertia, the latter results in higher cost. This problem, in addition to our prior discussion, makes the cost of a DC/DC converter reasonable.

4.2.3 Diesel Droop Factor

The governor shown in Figure 4.11 is responsible for regulating the active power and the frequency in convenient thermal generators. The basic relation, for describing its functionality, is introduced in (4.62) and is known as the droop equation, described in section 2.2.2. As mentioned previously, the frequency deviation is used to regulate the power. To decrease the undesirable frequency deviation, lower K_p should be used. This lower value becomes more interesting in microgrids with wind, in that the generated power and consequently the frequency are always changing.

$$P - P_0 = -\frac{1}{K_p}(\omega - \omega_0) \tag{4.62}$$

Although lower K_p will result in better frequency regulation in a steady-state, the dynamic behavior of a generator will become worse. As mentioned, this finding was also observed in inverter-based DGs, which share their power by the droop method.

This simplified model is used here to investigate the impact of virtual inertia on droop dynamic behavior. Figure 4.15 depicts the root locus of the system dominant poles when K_p is decreased. The red ones, representing the system without virtual inertia, move towards the RHP. That is, the system's dynamic behavior worsens as K_p is decreased, a finding that verifies the above discussion. After some points, the dominant poles pass the imaginary axis and the system becomes unstable.

The situation is significantly different when virtual inertia is implemented. Although decreasing K_p too much also leads to the system instability, it occurs much later than in the former case. In addition, decreasing K_p improves system behavior. It should be mentioned that, in Figure 4.15, a Super-Capacitor is used as the source of virtual inertia.

Implementing virtual inertia lets us choose K_p more freely to provide a better steady-state performance; in other words, such inertia decouples the steady and transient control parameters. As a result, it improves the system's steady-state behavior but is not incorporated directly in this mode.

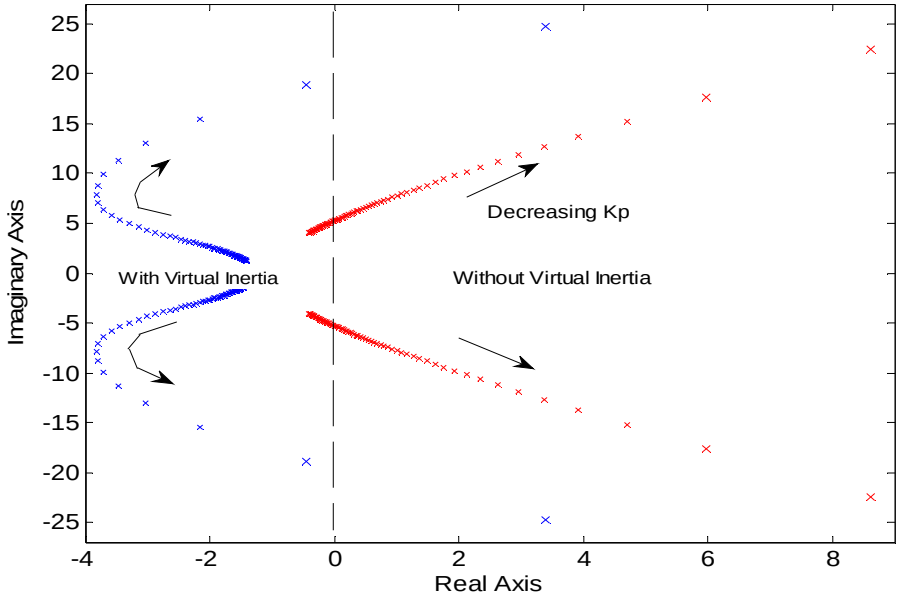

Figure 4.15 The Microgrid Dominant Poles' Root Locus when K_p is decreasing. Red ones describe the system without virtual inertia while the blue ones are for the system with virtual inertia.

4.3 Discussion

In this chapter, the impact of implementing virtual inertia in wind power is studied through a detailed model of wind power. To overcome its complexity, a simplified yet accurate version of the model is obtained and later used to construct the microgrid and study stability improvement in the presence of virtual inertia. Additionally, and based on the simplified model, the advantages and disadvantages of implementing virtual inertia using a Super-Capacitor or DFIG rotating mass are discussed in detail.

Chapter 5
Simulation Result

Time domain simulation is used to verify the situations discussed in the previous chapter, with two distinct scenarios being investigated. The first scenario deals with constant wind speed, and the second uses a real wind speed pattern. Each scenario consists of different cases.

The system shown in Fig. 4.1 is also used for the simulation. DG2, a conventional gas-turbine generator, is modeled based on details discussed in [44]. The droop and excitation system models are also included. Lines are modeled as lumped R-L and the loads as parallel R-L loads. Details of the loads are given in Appendix D. The Matlab/Simulink software package was used for this portion of the study.

5.1 Constant Wind Speed

First, wind speed is set as a constant to avoid any confusion. Since the analysis in the last section shows some dependency on wind speed, this part is divided into three different cases.

5.1.1 High Wind Speed

In this section, the wind speed is set constant at 11 m/sec. While all loads are connected, DG1 works at 1.52MW/0 MVAR and DG2 operates at 1.74MW and very close to the unity power factor. The rest of the loads are supplied by the grid. An intentional islanding takes place at t=2sec.

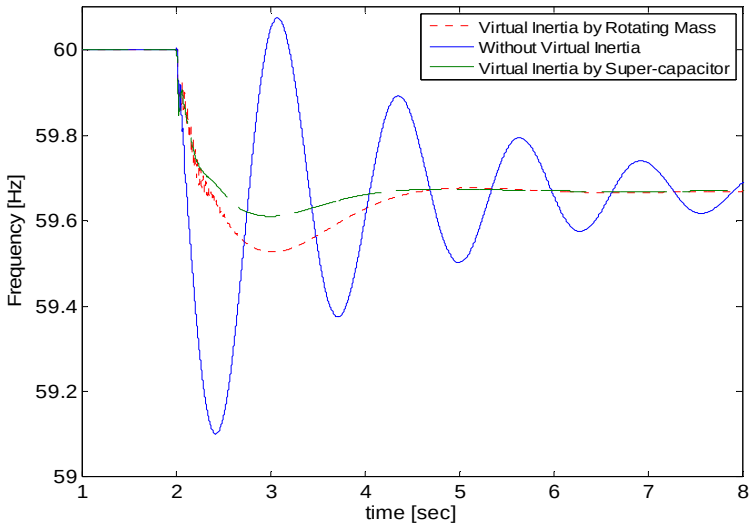

Figure 5.1 Frequency vs. time when wind speed is constantly 11m/sec. J_V for rotating mass and Super-Capacitor-based virtual inertia is the same.

The frequency is shown in Figure 5.1. As expected, virtual inertia significantly improves the frequency overshoot and settling time. It also verifies the previous analysis which claims that a Super-Capacitor as the source of virtual inertia could be more influential.

5.1.2 Low Wind Speed

In this case, the wind speed is 6m/sec. All microgrid loads except LP2 are disconnected. While DG2 works as in the previous case, DG1 output is 250KW/0MVAR before islanding. An intentional islanding takes place at t=2sec.

Figure 5.2 shows the frequency behaviour. As before, virtual inertia greatly improves the stability. It also shows that a Super-capacitor as the source can impact the system more significantly.

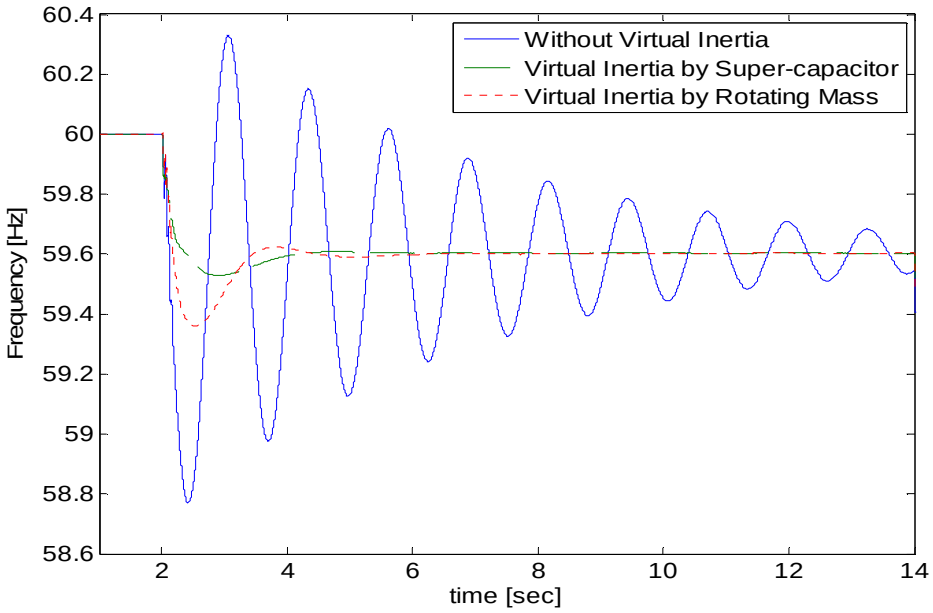

Figure 5.2 Frequency vs. time when wind speed is constantly 6m/sec. J_V for rotating mass and Super-capacitor-based virtual inertia is the same.

The remarkable point that can be concluded from the comparison between Figure 5.1 and Figure 5.2 is the dependence of the rotating-mass-based inertia on the DFIG initial rotating speed. Although the frequency overshoot in the high wind speed case is 42%, it reaches 60% in the low speed case. In contrast, in both of the Super-Capacitor-based virtual inertia cases, the overshoot is limited to 18%. This result verifies previous analyses and also shows that when a constant virtual inertia is utilized with a rotating-mass source, all wind speed probabilities should be considered in the design process.

5.1.3 Zero Wind Speed

When wind speed is lower than cut-in or higher than cut-out speed, wind power generator output decreases to zero. These situations are equivalent to and modeled as zero wind speed. Similar to the previous case, all microgrid loads except LP2 are disconnected, and DG2 works at 1.74MW and very close to unity power factor. DG1 output is 0MW/0MVAR. Figure 5.3 shows the microgrid frequency behavior when an intentional islanding occurs at t=2sec.

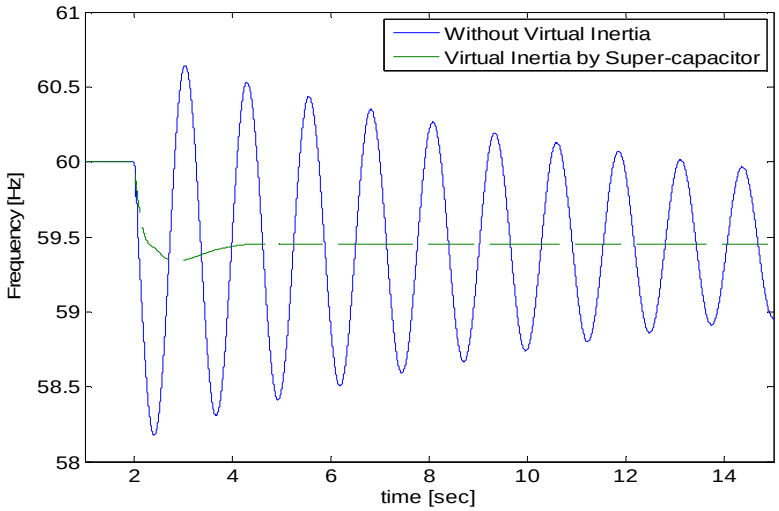

Figure 5.3 Frequency vs. time when wind speed is constantly 0m/sec. Implementing virtual inertia by the DFIG rotating mass in this condition is impossible

While implementing virtual inertia by the DFIG rotating mass is impossible due to zero rotating speed, the Super-Capacitor can still provide power to enhance the system's behavior. This feature seems very important, since this condition happens often in most wind power sites.

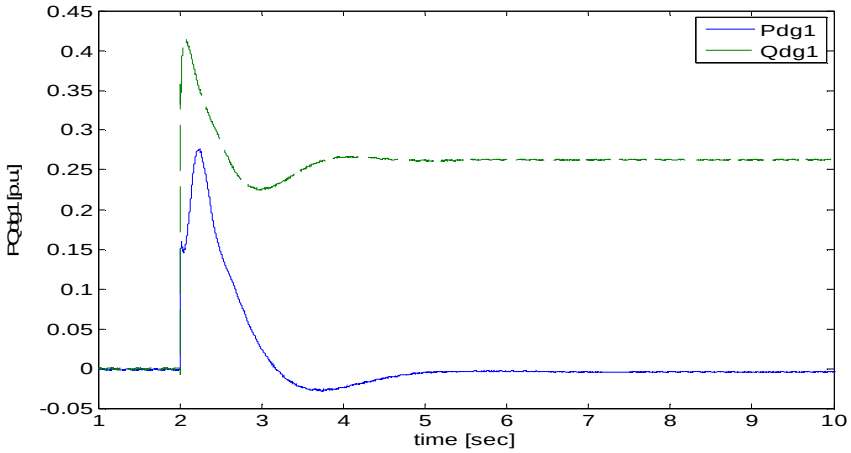

Figure 5.4 The DG1 active and reactive power output at zero wind speed with Super-Capacitor-based virtual inertia.

The output of DG1 when virtual inertia is implemented is shown in Figure 5.4. Although the wind speed is zero, it is used to regulate the reactive power and frequency. After islanding in steady-state because of losses in DFIG, a small amount of power is consumed by DG1, which is then used to generate reactive power. Ignoring this amount, DG1's active power output occurs because of the virtual inertia power generated by the super-capacitor connected to the DC-link. The maximum power generated because of virtual inertia is almost 0.28 p.u. This amount is very close to 0.30 p.u., which can be found based in Figure 4.14. The power mismatch at the moment of islanding is equal to the power supplied by the grid beforehand (0.39 p.u. in this case). This amount should be multiplied by 0.78, the maximum per-unit power generated for the 1 p.u. mismatch at J_V=14sec depicted in Figure 4.14. This clearly shows that the analytical method result is not far removed from the practical ones.

5.2 Variable Wind Speed

To make the system more practical, a real wind speed pattern derived from a real measured wind speed [45] is used.

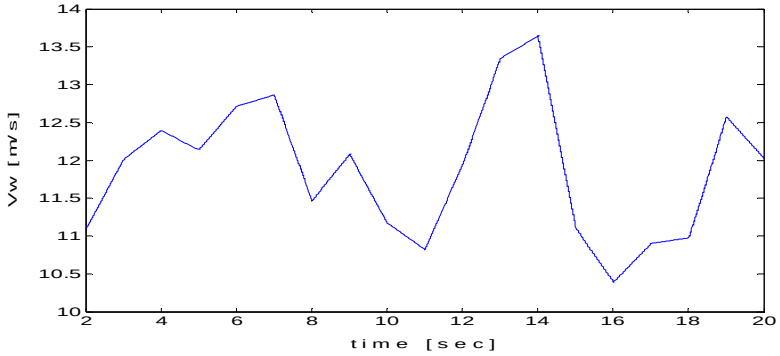

Figure 5.5 Real wind speed pattern

Islanding occurs at t=2sec, when the overall output of DFIG and back-to-back converter is 1.53MW at the unity power factor. The synchronous generator works at 1.74MW, very close to the unity power factor, while the rest of the loads are supplied by the main grid.

5.2.1 Implementing Virtual Inertia

The impact of using virtual inertia from different sources in a more realistic system is investigated here, with results shown in Figures 5.6 to 5.8. The governor of the diesel turbine has the same setting in all of the cases, so the frequency regulation differences are related to the virtual inertia.

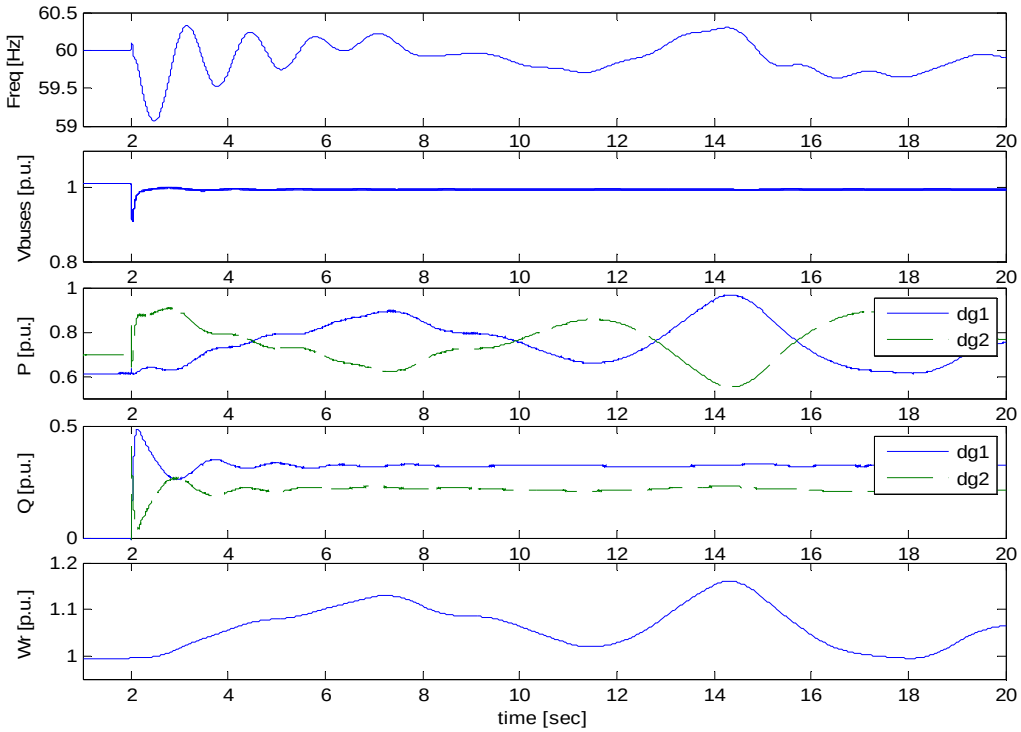

Figure 5.6 Intentional islanding without virtual inertia(K_p=2.5%)

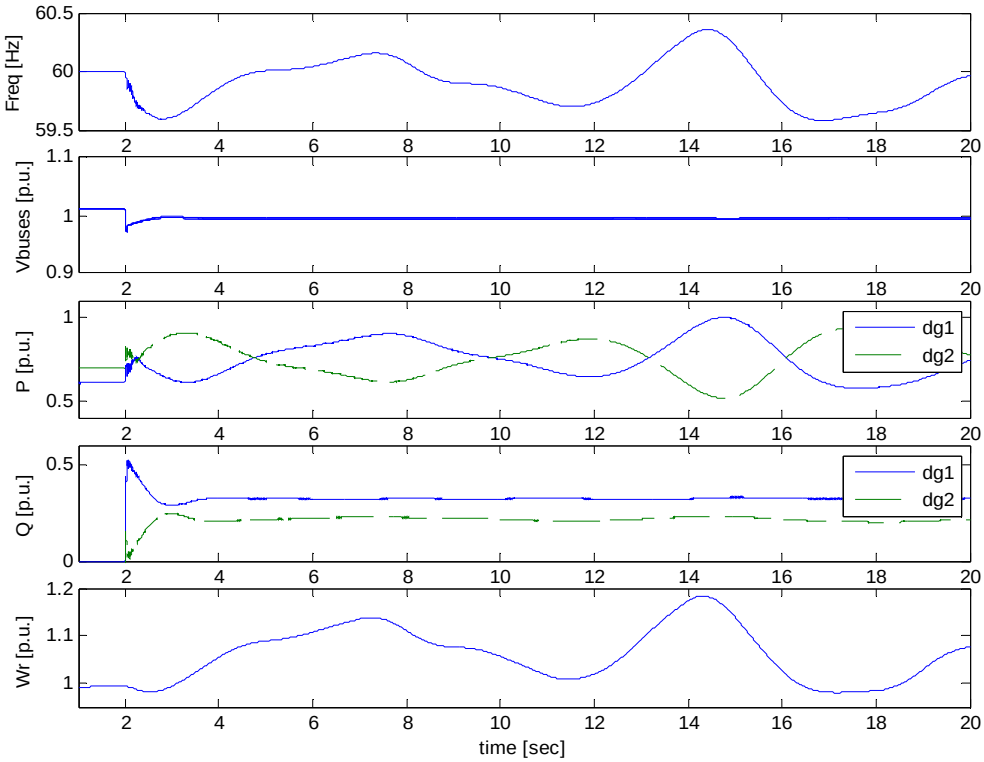

Figure 5.7 Intentional islanding with rotating-mass-based virtual inertia (K_p=2.5%)

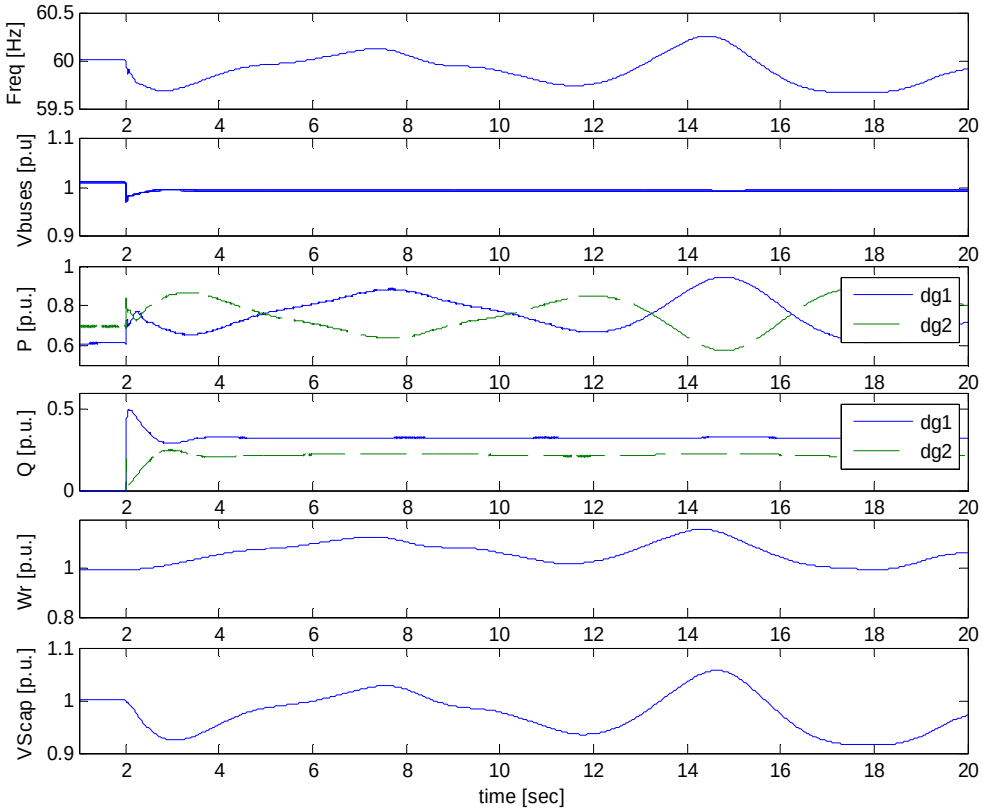

Figure 5.8 Intentional islanding with super-capacitor-based virtual inertia (K_p=2.5%)

The fluctuating wind speed results in variable DG1 output. As a result, the DG2 output and consequently the frequency should always change. While these changes are unavoidable (since a droop-based DG is used to compensate for wind), a comparison between curves shows that virtual inertia, either from a rotating-mass or a Super-Capacitor, could enhance frequency regulation. It is observed that for the similar amount of virtual inertia, a Super-Capacitor is more effective. While the Super-Capacitor performance is very obvious, the rotating-mass impact is not so clear. Comparing W_r (the DFIG rotational speed) in Figures 5.6 to 5.8 in the first seconds after islanding shows how rotating-mass-based virtual inertia provides energy to incorporate in frequency regulation.

For the sake of clarity, the frequency behaviors of all of these systems are shown in Figure 5.9. Although their behaviors after t=10sec are similar to each other, their performances in the first few cycles after islanding are quite different.

The other interesting observation in these figures concerns reactive power regulation. However the same strategy and parameters for controlling reactive power is used in all the cases, results show better regulation in the presence of virtual inertia. This is due to the low X/R ratio in the rural

network, which prevents the complete decoupling of active power/frequency and reactive power/voltage controls.

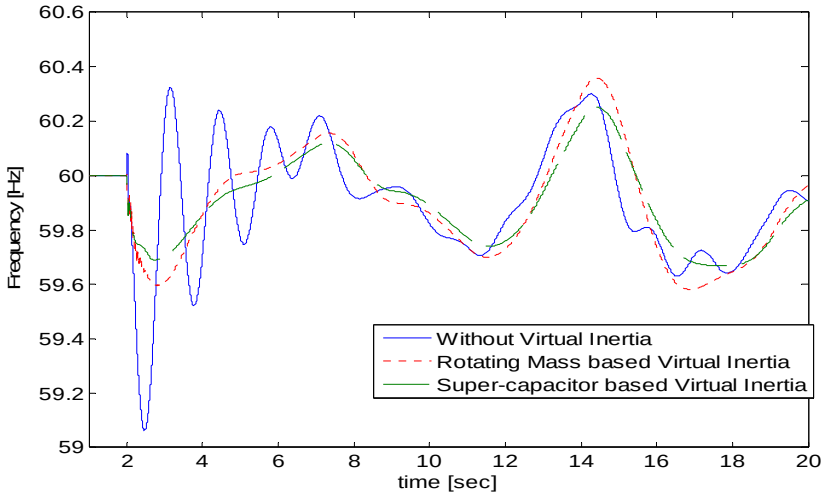

Figure 5.9 Intentional islanding with variable wind speed (Kp=2.5%)

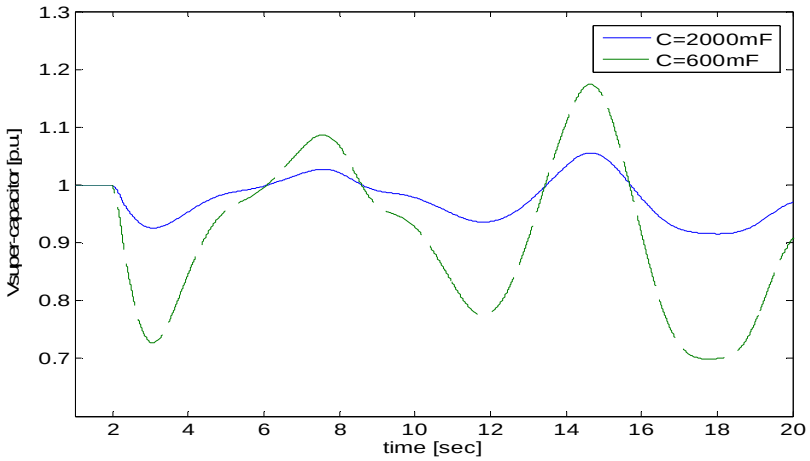

Figure 5.10 Super-Capacitor voltage when virtual inertia uses this source.

Another interesting point which should be mentioned here is the Super-Capacitor voltage. A comparison between the frequency and the Super-Capacitor voltage behavior in Figures 5.9 and 5.10 reveals the high degree of similarity between them, thus verifying the relation derived in (4.61).

5.2.2 Super-capacitor connection to DC-link

Up to this point in the chapter, the DC/DC converter was used to connect the Super-Capacitor to the DC-link in cases where the Super-Capacitor played the role of virtual inertia. Results related to the direct connection of the Super-Capacitor are shown in Figure 5.11. Comparing these results and

Figure 5.7 reveals a high level of similarity, showing the sufficiency of using one of these topologies in the other sections.

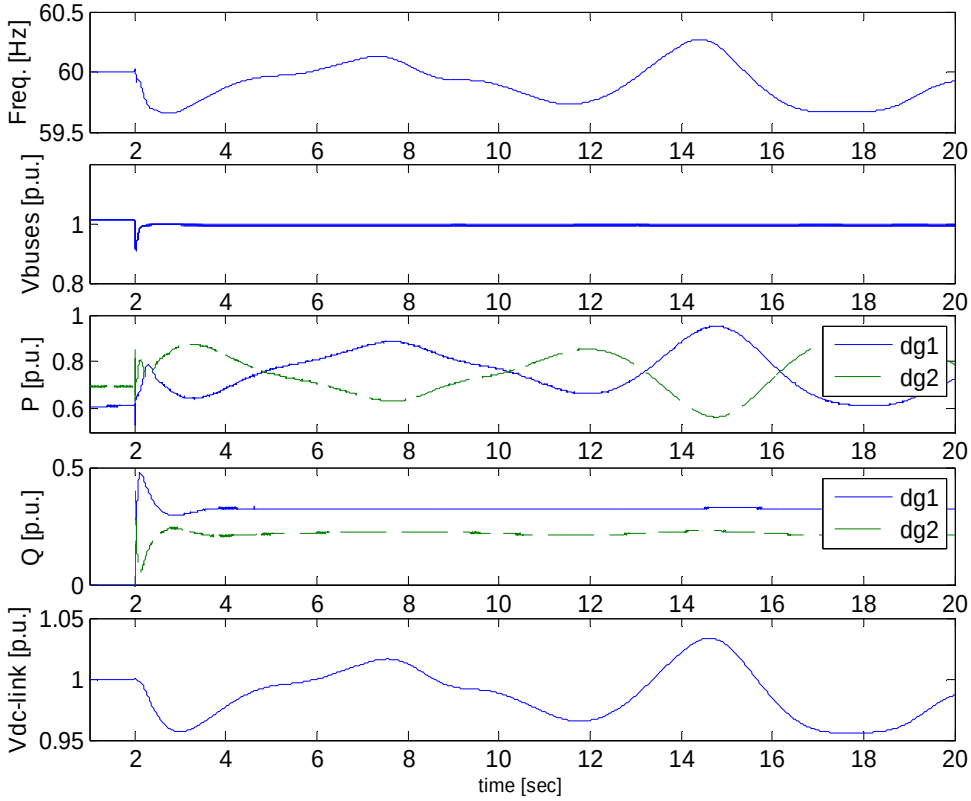

Figure 5.11 Super-Capacitor-based virtual inertia; Super-Capacitor directly connected to DC-link

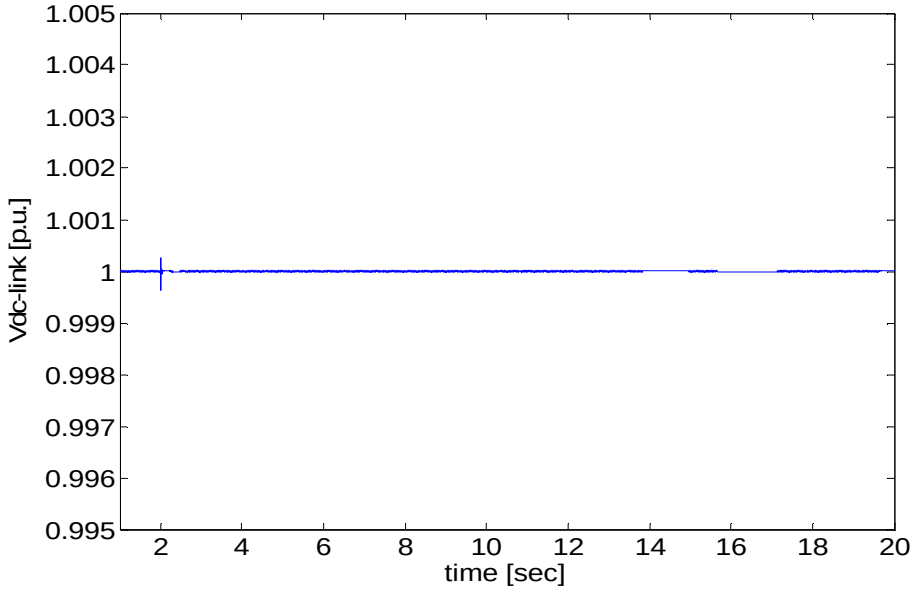

Figure 5.12 DC-link Voltage in Super-Capacitor-based virtual inertia: DC/DC converter is used

As mentioned previously, an important consideration about the direct connection of a Super-Capacitor is the DC-link voltage. While Figure 5.12 shows an almost constant voltage when using DC/DC converter, even with a 600mF Super-Capacitor, Figure 5.11 depicts a 0.1 per unit voltage fluctuation in the DC-link. Increasing the J_V to improve the frequency regulation or decreasing the C_{scap} to decrease the cost will result in higher fluctuations. Even with same amount of J_V or C_{scap} in cases of severe disturbance, the DC-link voltage is subject to high variations.

5.2.3 Compatibility

Using virtual inertia on both the rotating mass and the Super-Capacitor simultaneously presents no theoretical problems, since they are two completely separate sources. Time domain simulation also verifies this compatibility, as depicted in Figure 5.13.

Indeed, utilizing both sources at the same time may lead to a better solution. Using rotating mass may allow for choosing smaller amounts of virtual inertia on the Super-Capacitor, thus lowering the ratings of the Super-Capacitor, DC/DC converter and GSC. On the other hand, using Super-Capacitor-based virtual inertia may decrease system dependency on the DFIG initial rotating speed.

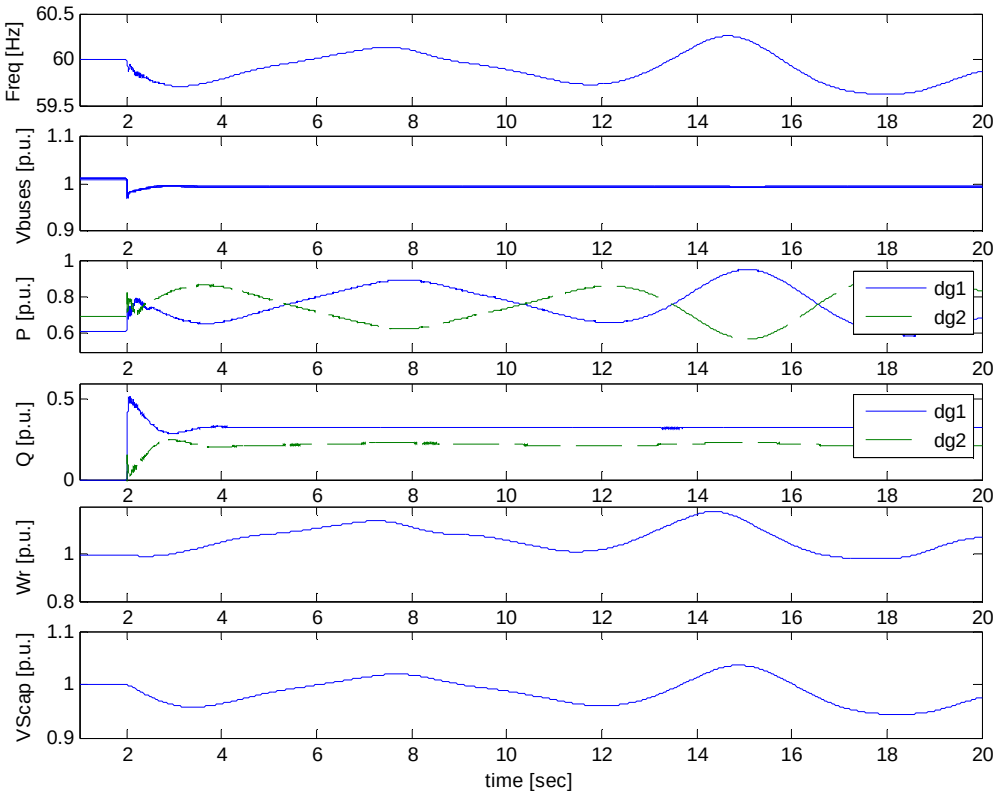

Figure 5.13 Intentional islanding with virtual inertia on both sources (K_p=2.5%)

5.2.4 Lower Diesel Droop Factor

While virtual inertia enhances frequency behavior in transient mode, the steady-state response of the system controlled by a droop-based governor still fluctuates widely, an undesirable trait. As discussed, for better long-term performance, K_p should be decreased, but lowering the K_p in the system without virtual inertia makes the system unstable. For instance, without virtual inertia, the system with K_p=1.25% becomes unstable in the case of an intentional islanding (see Figure 5.15). The presence of virtual inertia can change the situation and result in further decrease of K_p. Figure 5.14 shows the system with virtual inertia in which K_p is as low as 0.33%. Clearly, not only is the system stable, but the frequency fluctuation is much less.

The maximum frequency deviation in the system with K_p=0.33% after t=10sec is less than ±0.06Hz, while with K_p=2.5% for a similar time period is more than 0.36Hz. In other words, it proves the previous claim that virtual inertia can be used for a better steady-state performance in addition to its main functionality of system stabilization.

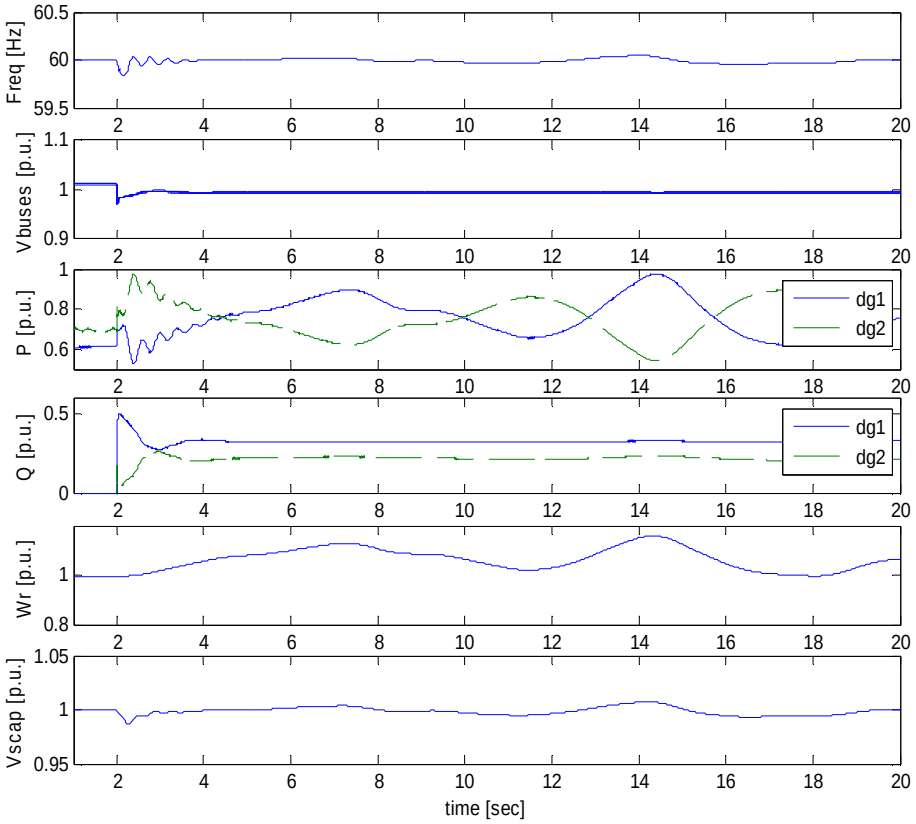

Figure 5.14 Intentional islanding with super-capacitor based virtual inertia and K_p=0.33%

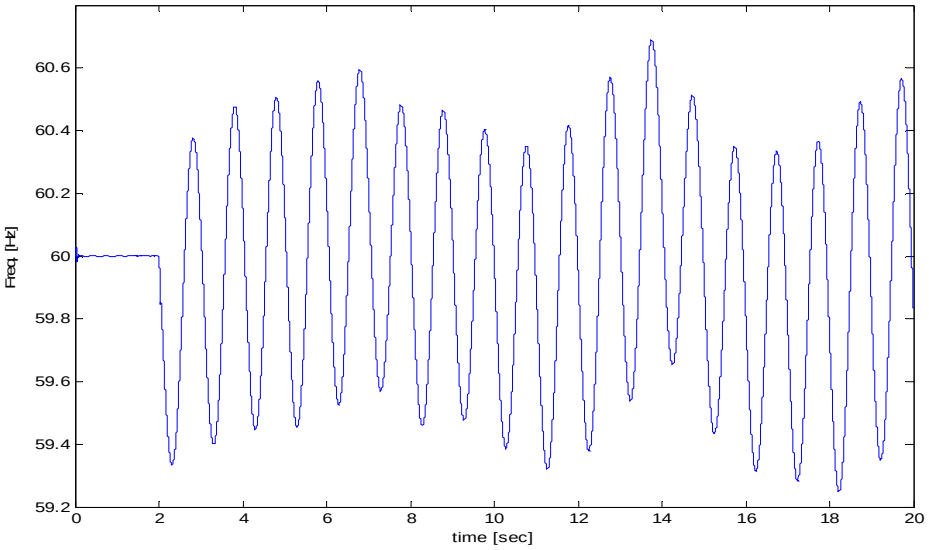

Figure 5.15 System frequency without virtual inertia and K_p=1.25%

5.3 Discussion

In this chapter, real-time simulation is used to verify discussions in the previous chapter. Wind speed is assumed constant to avoid any confusion, and the results of this case verify the dependence of rotating-mass-based virtual inertia on wind speed and Super-Capacitor-based virtual inertia independency.

As well, a variable wind speed pattern is used to produce more practical simulations. Also shown in this section is the relation between Super-Capacitor voltage and microgrid frequency, the advantages of utilizing DC/DC converter, the compatibility of rotating-mass-based and Super-Capacitor-based virtual inertia, and their impact on long-term frequency regulation.

Chapter 6
Conclusions and Future Work

6.1 Conclusions

Since virtual inertia does not participate in power sharing, no mass energy storage device is needed. This finding leads to economic advantages: either the rotating mass connected to the DFIG shaft or a Super-Capacitor connected a back-to-back converter DC-link could be used. Both of these sources are discussed in detail.

The modification needed in conventional wind power to incorporate each of the sources was explained. Eigen-value analysis was used to introduce a simplified model for a microgrid. This model shows the advantages and disadvantages of each inertia source.

Although virtual inertia based on any of these sources improves the system stability, their impacts are different. It was shown that while rotating-mass-based virtual inertia does not need any new part or de-rating, its performance is highly dependent on DFIG rotating speed at the disturbance moment. This rotating speed is a function of wind speed, which is notoriously unpredictable.

On the other hand, Super-Capacitor-based virtual inertia, which can improve system behavior much more and is independent of wind speed, needs an additional Super-Capacitor, a rerating of GSC, and possibly a DC/DC convertor. Several formulae and diagrams showing the relation of virtual inertia and size of these elements were introduced.

Modifications needed to connect the Super-Capacitor directly to the DC-link were discussed. It was shown that, despite removing the cost factor of a DC/DC converter, lower reliability and fluctuating DC-link voltage made this topology unpopular.

It was also discussed that while virtual inertia does not participate directly in long-term power and frequency regulation, it can influence the steady-state performance of the system by decoupling the steady-state and transient control parameters. Theoretical analyses and time domain simulation were used to verify the thesis's claims.

6.2 Future Work

Further study could involve the impact of virtual inertia on grid-connected microgrids that spend most of their time in this mode. As well, the response of virtual inertia to disturbances (e.g., switching) needs to be studied, as does the impact of such disturbances in the islanding mode of operation

To make the system more realistic, an unbalanced system with harmonics should be considered. Unbalancing and harmonics may have several effects on PLL, which is used as the core of virtual inertia. The compatibility of several DG units using virtual inertia is yet another area that requires more research.

Unlike real inertia, which is constant, virtual inertia can be easily changed and lead to optimized performance. Adaptive virtual inertia is also an interesting concept that warrants further investigation.

Appendix A

DFIG State-Space

By defining Γ as (4.1.3) and replacing T_e by its linearized representation, the DFIG state space equations could be shown as (4.1.4) to (4.1.8).

$$\Gamma = \begin{bmatrix} -(L_s + L_m) & 0 & L_m & 0 \\ 0 & -(L_s + L_m) & 0 & L_m \\ -L_m & 0 & (L_r + L_m) & 0 \\ 0 & -L_m & 0 & (L_r + L_m) \end{bmatrix} \tag{A.1}$$

$$\dot{x}_{dfig} = A_{dfig} x_{dfig} + B_{vs,dfig} \begin{bmatrix} \Delta v_{qs} \\ \Delta v_{ds} \end{bmatrix} + B_{vr,dfig} \begin{bmatrix} \Delta v'_{qr} \\ \Delta v'_{dr} \end{bmatrix} + B_{w,dfig} [\Delta\omega] + B_{tm,dfig} [\Delta T_m] \tag{A.2}$$

$$\Delta P_r = C_{dfig} x_{dfig} + D_{vs,dfig} \begin{bmatrix} \Delta v_{qs} \\ \Delta v_{ds} \end{bmatrix} + D_{vr,dfig} \begin{bmatrix} \Delta v'_{qr} \\ \Delta v'_{dr} \end{bmatrix} + D_{w,dfig} [\Delta\omega] + D_{tm,dfig} [\Delta T_m] \tag{A.3}$$

$$x_{dfig} = \begin{bmatrix} \Delta i_{qs} \\ \Delta i_{ds} \\ \Delta i'_{qr} \\ \Delta i'_{dr} \\ \Delta\omega_r \end{bmatrix} \tag{A.4}$$

$$A_{dfig} = \begin{bmatrix} \Gamma^{-1} \begin{bmatrix} -R_s & -\omega_0(L_s + L_m) & 0 & \omega_0 L_m \\ \omega_0(L_s + L_m) & -R_s & -\omega_0 L_m & 0 \\ 0 & -(\omega_0 - \omega_r)L_m & R'_r & (\omega_0 - \omega_r)(L_r + L_m) \\ (\omega_0 - \omega_r)L_m & 0 & -(\omega_0 - \omega_r)(L_r + L_m) & R'_r \end{bmatrix} & \Gamma^{-1} \begin{bmatrix} 0 \\ 0 \\ \Delta\psi'_{dr0} \\ -\Delta\psi'_{dr0} \end{bmatrix} \\ -\frac{L_m}{2H_{DG1}} \begin{bmatrix} I_{dr0} & -I_{qr0} & -I_{ds0} & I_{qs0} \end{bmatrix} & 0 \end{bmatrix} \tag{A.5}$$

If DFIG is connected to the network via reactance X_N, then the relation between the v_s, v_b and i_x is described by (A.6).

$$\begin{bmatrix} v_{sq} \\ v_{sd} \end{bmatrix} = \begin{bmatrix} 0 & -\omega_0 L_N \\ \omega_0 L_N & 0 \end{bmatrix} \begin{bmatrix} i_{xq} \\ i_{xd} \end{bmatrix} + \begin{bmatrix} L_N & 0 \\ 0 & L_N \end{bmatrix} \frac{d}{dt} \begin{bmatrix} i_{xq} \\ i_{xd} \end{bmatrix} + \begin{bmatrix} v_{bd} \\ v_{bq} \end{bmatrix} \tag{A.6}$$

Without loss of generality, (A.6) could be represented as (A.7).

$$\begin{bmatrix} v_{sq} \\ v_{sd} \end{bmatrix} = \begin{bmatrix} 0 & -\omega_0 L_N & 0 & 0 \\ \omega_0 L_N & 0 & 0 & 0 \\ 0 & 0 & 0 & 0 \\ 0 & 0 & 0 & 0 \end{bmatrix} \begin{bmatrix} \Delta i_{qs} \\ \Delta i_{ds} \\ \Delta i'_{qr} \\ \Delta i'_{dr} \end{bmatrix} + \begin{bmatrix} L_N & 0 & 0 & 0 \\ 0 & L_N & 0 & 0 \\ 0 & 0 & 0 & 0 \\ 0 & 0 & 0 & 0 \end{bmatrix} \frac{d}{dt} \begin{bmatrix} \Delta i_{qs} \\ \Delta i_{ds} \\ \Delta i'_{qr} \\ \Delta i'_{dr} \end{bmatrix} + \begin{bmatrix} v_{bd} \\ v_{bq} \end{bmatrix} \tag{A.7}$$

By replacing v_s in (4.1.1) with the right side of (A.7), new equations will be derived.

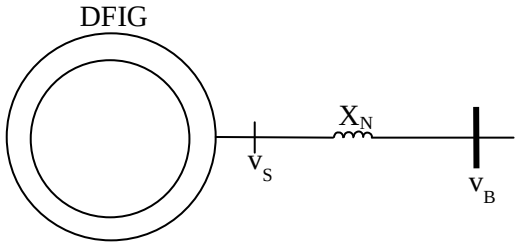

$$\Gamma_{new} = \begin{bmatrix} -(L_s + L_m + L_N) & 0 & L_m & 0 \\ 0 & -(L_s + L_m + L_N) & 0 & L_m \\ -L_m & 0 & (L_r + L_m) & 0 \\ 0 & -L_m & 0 & (L_r + L_m) \end{bmatrix} \tag{A.8}$$

$$A_{dfig}^{new} = \begin{bmatrix} \Gamma_{new}^{-1} \begin{bmatrix} -R_s & -\omega_0(L_s + L_m + L_N) & 0 & \omega_0 L_m \\ \omega_0(L_s + L_m + L_N) & -R_s & -\omega_0 L_m & 0 \\ 0 & -(\omega_0 - \omega_r)L_m & R'_r & (\omega_0 - \omega_r)(L_r + L_m) \\ (\omega_0 - \omega_r)L_m & 0 & -(\omega_0 - \omega_r)(L_r + L_m) & R'_r \end{bmatrix} & \Gamma_{new}^{-1} \begin{bmatrix} 0 \\ 0 \\ \Delta\psi'_{dr0} \\ -\Delta\psi'_{dr0} \end{bmatrix} \\ -\frac{L_m}{2H_{DG1}} \begin{bmatrix} I_{dr0} & -I_{qr0} & -I_{ds0} & I_{qs0} \end{bmatrix} & 0 \end{bmatrix} \tag{A.9}$$

On the other hand, by introducing matrices $E_{1,vs}$ and $E_{2,vs}$, as shown below, and replacing the derivative term in (A.8) with its equivalents, v_s now can be defined based on a DFIG state-space model.

$$E_{1,vs} = \begin{bmatrix} 0 & -\omega_0 L_N & 0 & 0 & 0 \\ \omega_0 L_N & 0 & 0 & 0 & 0 \\ 0 & 0 & 0 & 0 & 0 \\ 0 & 0 & 0 & 0 & 0 \\ 0 & 0 & 0 & 0 & 0 \end{bmatrix}, \quad E_{2,vs} = \begin{bmatrix} L_N & 0 & 0 & 0 & 0 \\ 0 & L_N & 0 & 0 & 0 \\ 0 & 0 & 0 & 0 & 0 \\ 0 & 0 & 0 & 0 & 0 \\ 0 & 0 & 0 & 0 & 0 \end{bmatrix} \tag{A.10}$$

$$\begin{bmatrix} v_{sq} \\ v_{sd} \end{bmatrix} = (E_{1,vs} + E_{2vs} A_{dfig}^{new}) x_{dfig} + (E_{2vs} B_{vb,dfig}^{new} + \begin{bmatrix} 1 & 0 \\ 0 & 1 \end{bmatrix}) \begin{bmatrix} v_{bd} \\ v_{bq} \end{bmatrix} + E_{2vs} B_{vr,dfig}^{new} \begin{bmatrix} \Delta v'_{qr} \\ \Delta v'_{dr} \end{bmatrix} + E_{2vs} B_{w,dfig}^{new} [\Delta\omega] + E_{2vs} B_{tm,dfig}^{new} [\Delta T_m] \quad \text{(A.11)}$$

Appendix B

RSC State-Space

$$A_{rsc}=\begin{bmatrix}0 & 0 & K_{ivr}\\ 0 & 0 & 0\\ 0 & 0 & 0\end{bmatrix},\ B_{dfig,rsc}=\begin{bmatrix}0 & 0 & -1 & 0 & 0\\ 0 & 0 & 0 & -1 & \dfrac{2K_{OPT}\omega_0\omega_{r0}(L_s+L_m)}{L_mV_{db0}}\\ 0 & 0 & 0 & 0 & 0\end{bmatrix} \tag{B.1}$$

$$B_{vs,rsc}=\begin{bmatrix}\dfrac{K_{pvr}V_{qs0}}{V_{ds0}^2+V_{qs0}^2} & \dfrac{K_{pvr}V_{ds0}}{V_{ds0}^2+V_{qs0}^2}\\ 0 & 0\\ \dfrac{V_{qs0}}{V_{ds0}^2+V_{qs0}^2} & \dfrac{V_{ds0}}{V_{ds0}^2+V_{qs0}^2}\end{bmatrix},\ B_{vb,rsc}=\begin{bmatrix}0 & -\dfrac{1}{\omega_0L_m}\\ 0 & -\dfrac{K_{OPT}\omega_0\omega_{r0}^2(L_s+L_m)}{L_mV_{db0}^2}\\ 0 & 0\end{bmatrix},\ B_{vDC,rsc}=\begin{bmatrix}0\\0\\0\end{bmatrix} \tag{B.2}$$

$$C_{rsc}=0.5V_{DC0}\begin{bmatrix}K_{ir} & 0 & K_{pr}K_{ivr}\\ 0 & K_{ir} & 0\end{bmatrix},\ D_{dfig,rsc}=0.5V_{DC0}\begin{bmatrix}0 & 0 & -K_{pr} & 0 & 0\\ 0 & 0 & 0 & -K_{pr} & \dfrac{2K_{pr}K_{OPT}\omega_0\omega_{r0}(L_s+L_m)}{L_mV_{db0}}\end{bmatrix} \tag{B.3}$$

$$D_{vs,rsc}=0.5V_{DC0}\begin{bmatrix}\dfrac{K_{pr}K_{pvr}V_{qs0}}{V_{ds0}^2+V_{qs0}^2} & \dfrac{K_{pr}K_{pvr}V_{ds0}}{V_{ds0}^2+V_{qs0}^2}\\ 0 & 0\end{bmatrix},\ D_{vb,rsc}=0.5V_{DC0}\begin{bmatrix}0 & -\dfrac{K_{pr}}{\omega_0L_m}\\ 0 & -\dfrac{K_{pr}K_{OPT}\omega_0\omega_{r0}^2(L_s+L_m)}{L_mV_{db0}^2}\end{bmatrix} \tag{B.4}$$

$$D_{vDC,rsc}=\begin{bmatrix}0.5M_{qr0}\\ 0.5M_{dr0}\end{bmatrix} \tag{B.5}$$

Appendix C

GSC State-Space

$$A_{gsc}=\begin{bmatrix} 0 & 0 & 0 & 0 & -V_{db0} & V_{qb0} \\ 0 & 0 & 0 & 0 & 0 & 0 \\ K_{igq} & 0 & 0 & 0 & -1-K_{igq}V_{db0} & K_{igq}V_{qb0} \\ 0 & K_{igd} & 0 & 0 & 0 & -1 \\ \frac{V_{DC0}K_{pc}K_{igq}}{2L_s} & 0 & -\frac{V_{DC0}K_{ic}}{2L_s} & 0 & -\frac{V_{DC0}K_{ic}(K_{pc}+K_{pc}K_{igq}V_{db0})}{2L_s} & -\omega_0-\frac{V_{DC0}K_{ic}(X_s+K_{pc}K_{igq}V_{qb0})}{2L_s} \\ 0 & \frac{V_{DC0}K_{pc}K_{igq}}{2L_s} & 0 & -\frac{V_{DC0}K_{ic}}{2L_s} & \omega_0-\frac{V_{DC0}K_{ic}X_s}{2L_s} & -\frac{V_{DC0}K_{ic}K_{pc}}{2L_s} \end{bmatrix} \quad \text{(C.1)}$$

$$B_{vb,gsc}=\begin{bmatrix} I_{cd0} & -I_{qc0} \\ 0 & 0 \\ K_{pgq}I_{cd0} & K_{pgq}I_{cq0} \\ 0 & 0 \\ \frac{2+V_{DC0}K_{pgq}I_{cd0}}{2L_s} & \frac{2+V_{DC0}K_{pgq}I_{cd0}}{2L_s} \\ 0 & 0 \end{bmatrix},\ B_{vDC,gsc}=\begin{bmatrix} 0 \\ -1 \\ 0 \\ 0 \\ \frac{0.5M_{qc0}}{-L_s} \\ \frac{0.5M_{qc0}}{-L_s} \end{bmatrix},\ B_{\omega,gsc}=\frac{1}{L}\begin{bmatrix} 0 \\ 0 \\ 0 \\ 0 \\ -I_{cd0} \\ I_{cq0} \end{bmatrix}$$

(C.2)

$$C_{gsc}=\begin{bmatrix} 0 & 0 & 0 & 0 & V_{bq0} & V_{bd0} \end{bmatrix},\ D_{vb,gsc}=\begin{bmatrix} I_{cq0} & I_{cd0} \end{bmatrix},\ D_{vDC,gsc}=0,\ D_{w,gsc}=0 \quad \text{(C.3)}$$

Appendix D

The model details

Table D.1 The model loads

Load Name	Corresponding Bus	P(KW)	Q(KVAR)
LP1	4	47.50	15.61
LP2	5	2565.0	843.06
LP3	6	289.75	95.24
LP4	7	152	49.96
LP5	8	517.75	170.18
LP6	8	194.75	64.01
LP7	2	7155.0	2566.71
LP8	2	3348.8	1100.7
LP9	3	1071.75	621.95

Table D.2 The model connections

From	To	R(Ω)	X(Ω)
1	2	1.096	2.710
2	3	0.232	0.573
3	4	1.277	3.157
4	5	0.066	0.089
5	6	0. 675	0.909
6	7	0.567	0.764
7	8	0.738	0.993
4	LP1	1.500	0.680
5	LP2	1.631	2.706
6	LP3	0.853	1.148
7	LP4	0.663	0.582
8	LP5	0.884	1.190
8	LP6	0.817	0.718

DG1 Parameters :

DFIG :

2.5MVA, V_n=690V, R_s=0.01pu, X_s=0.1pu, R_r=0.01pu, X_r=0.1pu, X_m=3pu, Number of poles=4, ω_n=1800rpm.

RSC controller :

$K_{pd}=K_{qd}$=0.5, $K_{id}=K_{iq}$=30, K_{opt}=0.628.

GSC Power controller:

J=250, ω_0=377, K_{pll}=120, K_{ill}=500, $K_v(s)=\frac{50s+5}{s}$.

DG2 Parameters:

Synchronous Generator:

2.5MVA, V_n=11KV, R_s=0.0036pu, X_d=1.56pu, X'_d=0.29pu, X''d=0.17pu, X_q=1.07pu, X'_q=0.035pu, X''_q=0.17, X_l=0.055pu, T'_d=0.035s, T''_d=0.037s, H=1.5s.

AVR Parameters: K_A=400, T_A=0.02

Diesel Turbine: Total time constant is almost 450ms

Bibliography

[1] E. Carpaneto, G. Chicco, A, Prunotto, " Reliability of Reconfigurable Distribution Systems Including Distributed Generation", *9th International Conference on probabilistic Method Applied to Power Systems, KTH, Stockholm, Sweden, June 11-15, 2006*, pp. 1-6.

[2] M. H. Nehrir, C. Wang, S. R. Guda, "Alternative Energy Distributed Generation: Need for Multi-Source Operation", *38th North America Power Symposium, NAPS 2006*, pp. 547-551.

[3] M. Shahabi, M. R. Haghifam, M. Mohamadian and S. A. Nabavi-Niaki, "Microgrid Dynamic Performance Improvement Using a Doubly Fed Induction Wind Generator," *IEEE Transactions on Energy Conversion*, vol. 24, pp. 137-145, 2009.

[4] M. H. J. Bollen, Y. Sun, G. W. Ault, "Reliability of Distribution Networks With Der Including Intentional Islanding", *International Conference on Future Power Systems*, 2005, pp. 1-6.

[5] Y. Mohamed and E. F. El-Saadany, "Adaptive Decentralized Droop Controller to Preserve Power Sharing Stability of Paralleled Inverters in Distributed Generation Microgrids," *IEEE Transactions on Power Electronics*, vol. 23, pp. 2806-2816, 2008.

[6] F. Katiraei, M. R. Iravani and P. W. Lehn, "Small-signal dynamic model of a micro-grid including conventional and electronically interfaced distributed resources," *Generation, Transmission & Distribution, IET*, vol. 1, pp. 369-378, 2007.

[7] S. K. Mazumder, K. Acharya and M. Tahir, ""Wireless" control of spatially distributed power electronics," in *Twentieth Annual IEEE Applied Power Electronics Conference and Exposition, APEC*, 2005, pp. 75-81 Vol. 1.

[8] A. Tuladhar, H. Jin, T. Unger and K. Mauch, "Parallel operation of single phase inverter modules with no control interconnections," in *Twelfth Annual Applied Power Electronics Conference and Exposition, 1997. APEC '97 Conference Proceedings*, 1997, pp. 94-100 vol.1.

[9] N. Pogaku, M. Prodanovic and T. C. Green, "Modeling, Analysis and Testing of Autonomous Operation of an Inverter-Based Microgrid," *IEEE Transactions on Power Electronics*, vol. 22, pp. 613-625, 2007.

[10] A. Tuladhar, H. Jin, T. Unger and K. Mauch, "Control of parallel inverters in distributed AC power systems with consideration of the line impedance effect," in *Thirteenth Annual Applied Power Electronics Conference and Exposition, APEC '98. Conference Proceedings*, 1998, pp. 321-328 vol.1.

[11] M. Griffiths and C. Coates, "Behavior of microgrids in the presence of unbalanced loads," in *Power Engineering Conference, AUPEC. Australasian Universities*, 2007, pp. 1-5.

[12] F. Katiraei and M. R. Iravani, "Power Management Strategies for a Microgrid With Multiple Distributed Generation Units," *IEEE Transactions on Power Systems,* vol. 21, pp. 1821-1831, 2006.

[13] K. De Brabandere, B. Bolsens, J. Van den Keybus, A. Woyte, J. Driesen and R. Belmans, "A Voltage and Frequency Droop Control Method for Parallel Inverters," *IEEE Transactions on Power Electronics,* vol. 22, pp. 1107-1115, 2007.

[14] R. Majumder, A. Ghosh, G. Ledwich and F. Zare, "Load sharing and power quality enhanced operation of a distributed microgrid," *Renewable Power Generation, IET,* vol. 3, pp. 109-119, 2009.

[15] R. Majumder, A. Ghosh, G. Ledwich and F. Zare, "Stability analysis and control of multiple converter based autonomous microgrid," in *IEEE International Conference on Control and Automation, ICCA,* 2009, pp. 1663-1668.

[16] Tzung-Lin Lee and Po-Tai Cheng, "Design of a New Cooperative Harmonic Filtering Strategy for Distributed Generation Interface Converters in an Islanding Network," *IEEE Transactions on Power Electronics,* vol. 22, pp. 1919-1927, 2007.

[17] U. Borup, F. Blaabjerg and P. N. Enjeti, "Sharing of nonlinear load in parallel-connected three-phase converters," *IEEE Transactions on Industry Applications,* vol. 37, pp. 1817-1823, 2001.

[18] J. M. Guerrero, L. G. de Vicuna, J. Matas, M. Castilla and J. Miret, "A wireless controller to enhance dynamic performance of parallel inverters in distributed generation systems," *IEEE Transactions on Power Electronics,* vol. 19, pp. 1205-1213, 2004.

[19] J. M. Guerrero, J. Matas, Luis Garcia de Vicuna, M. Castilla and J. Miret, "Decentralized Control for Parallel Operation of Distributed Generation Inverters Using Resistive Output Impedance," *IEEE Transactions on Industrial Electronics,* vol. 54, pp. 994-1004, 2007.

[20] Xuan Zhang, Jinjun Liu, Ting Liu and Linyuan Zhou, "A novel power distribution strategy for parallel inverters in islanded mode microgrid," in *Applied Power Electronics Conference and Exposition (APEC), Twenty-Fifth Annual IEEE,* 2010, pp. 2116-2120.

[21] F. A. Bhuiyan and A. Yazdani, "Multimode Control of a DFIG-Based Wind-Power Unit for Remote Applications," *IEEE Transactions on Power Delivery,* vol. 24, pp. 2079-2089, 2009.

[22] T. Bhattacharya and L. Umanand, "Negative sequence compensation within fundamental positive sequence reference frame for a stiff micro-grid generation in a wind power system using slip ring induction machine," *Electric Power Applications, IET,* vol. 3, pp. 520-530, 2009.

[23] Wang Qi, Chen Xiao-hu, Fei Wan-min and Ji Yan-chao, "Study of brushless doubly-fed control for VSCF wind power generation system connected to grid," in *Third International Conference on Electric Utility Deregulation and Restructuring and Power Technologies, DRPT*, 2008, pp. 2453-2458.

[24] B. H. Chowdhury, H. T. Ma and N. Ardeshna, "The challenge of operating wind power plants within a microgrid framework," in *Power and Energy Conference at Illinois (PECI)*, 2010, pp. 93-98

[25] L. Sovannarith and N. Hoonchareon, "Stability of the micro-grid with wind power generation," in *IEEE International Conference on Sustainable Energy Technologies, ICSET*, 2008, pp. 1087-1092.

[26] M. Fazeli, G. M. Asher, C. Klumpner and Liangzhong Yao, "Novel Integration of DFIG-Based Wind Generators within Microgrids," *IEEE Transactions on Energy Conversion*, vol. 26, pp. 840-850, 2011.

[27] C. Abbey and G. Joos, "Supercapacitor Energy Storage for Wind Energy Applications," *IEEE Transactions on Industry Applications*, vol. 43, pp. 769-776, 2007.

[28] Y. M. Atwa and E. F. El-Saadany, "Reliability Evaluation for Distribution System With Renewable Distributed Generation During Islanded Mode of Operation," *IEEE Transactions on Power Systems*, vol. 24, pp. 572-581, 2009.

[29] Y. M. Atwa, E. F. El-Saadany and A. -. Guise, "Supply Adequacy Assessment of Distribution System Including Wind-Based DG During Different Modes of Operation," *IEEE Transactions on Power Systems*, vol. 25, pp. 78-86, 2010.

[30] Seon-Ju Ahn, Jin-Woo Park, Il-Yop Chung, Seung-Il Moon, Sang-Hee Kang and Soon-Ryul Nam, "Power-Sharing Method of Multiple Distributed Generators Considering Control Modes and Configurations of a Microgrid," *IEEE Transactions on Power Delivery*, vol. 25, no. 3, pp. 2007-2016, 2010.

[31] E. Omine, T. Senjyu, E. B. Muhando, A. Yona, H. Sekine, T. Funabashi and A. Y. Saber, "Coordinated control of battery energy storage system and diesel generator for isolated power system stabilization," in *IEEE 2nd International Power and Energy Conference, PECon*, 2008, pp. 925-930.

[32] T. Senjyu, E. Omine, M. Tokudome, Y. Yonaha, T. Goya, A. Yona and T. Funabashi, "Frequency control strategy for parallel operated battery systems based on droop characteristics

by applying H∞ control theory," in *Transmission & Distribution Conference & Exposition: Asia and Pacific*, 2009, pp. 1-4.

[33] Y. A. -. I. Mohamed and E. F. El-Saadany, "A Robust Natural-Frame-Based Interfacing Scheme for Grid-Connected Distributed Generation Inverters," *IEEE Transactions on Energy Conversion*, vol. 26, no. 3, pp. 728-736, 2011.

[34] Y. Abdel-Rady Ibrahim Mohamed, E. F. El-Saadany and M. Salama, "Adaptive Grid-Voltage Sensorless Control Scheme for Inverter-Based Distributed Generation," *IEEE Transactions on Energy Conversion*, vol. 24, no. 3, pp. 683-694, 2009.

[35] K. Visscher and S. W. H. De Haan, "Virtual synchronous machines (VSG's) for frequency stabilisation in future grids with a significant share of decentralized generation," in *SmartGrids for Distribution, IET-CIRED. CIRED Seminar*, 2008, pp. 1-4.

[36] J. Driesen and K. Visscher, "Virtual synchronous generators," in *IEEE Power and Energy Society General Meeting - Conversion and Delivery of Electrical Energy in the 21st Century*, 2008, pp. 1-3.

[37] M. P. N. van Wesenbeeck, S. W. H. de Haan, P. Varela and K. Visscher, "Grid tied converter with virtual kinetic storage," in *PowerTech, IEEE Bucharest*, 2009, pp. 1-7.

[38] J. Ekanayake and N. Jenkins, "Comparison of the response of doubly fed and fixed-speed induction generator wind turbines to changes in network frequency," *IEEE Transactions on Energy Conversion*, vol. 19, pp. 800-802, 2004.

[39] Qing-Chang Zhong and G. Weiss, "Synchronverters: Inverters That Mimic Synchronous Generators," *IEEE Transactions on Industrial Electronics*, vol. 58, pp. 1259-1267, 2011.

[40] J. Ekanayake, Lee Holdsworth and N. Jenkins, "Control of DFIG wind turbines," *Power Engineer*, vol. 17, pp. 28-32, 2003.

[41] M. Torres and L. A. C. Lopes, "Virtual synchronous generator control in autonomous wind-diesel power systems," in *Electrical Power & Energy Conference (EPEC), IEEE*, 2009, pp. 1-6.

[42] J. G. Slootweg, H. Polinder and W. L. Kling, "Dynamic modelling of a wind turbine with doubly fed induction generator," in *Power Engineering Society Summer Meeting, 2001. IEEE*, 2001, pp. 644-649 vol.1.

[43] P. Krause, O. Wasynczuk, S. Sudhoff, *Analysis of Electic Machinery and Drive System*, Willy-IEEE Press, 2002.

[44] Se-Kyo Chung, "A phase tracking system for three phase utility interface inverters," *IEEE Transactions on Power Electronics*, vol. 15, pp. 431-438, 2000.

[45] P. C. Kundur, *Power System Stability and Control*. New York; Toronto: McGraw-Hill, 1994.

[46] Database of wind characteristics located at DTU, Denmark. [Online]. Available: http://www.winddata.com